Microphysical Process Comparison of Three Microphysics Parameterization Schemes in the WRF Model for an Idealized Squall-Line Case Study

J.-W. BAO

NOAA/Earth System Research Laboratory, Boulder, Colorado

S. A. MICHELSON AND E. D. GRELL

NOAA/Earth System Research Laboratory, and CIRES, University of Colorado Boulder, Boulder, Colorado

(Manuscript received 17 July 2018, in final form 29 May 2019)

ABSTRACT

Three bulk microphysics schemes with different complexities in the Weather Research and Forecasting Model are compared in terms of the individual microphysical process terms of the hydrometeor mass and number mixing ratio tendency equations in an idealized 2D squall-line case. Through evaluation of these process terms and of hydrometeor size distributions, it is shown that the differences in the simulated population characteristics of snow, graupel, and rainwater are the prominent factors contributing to the differences in the development of the simulated squall lines using these schemes. In this particular case, the gust front propagation speed produced by the Thompson scheme is faster than in the other two schemes during the first 2 h of the simulation because it has a larger dominant graupel size. After 2 h into the simulation, the initially less intense squall lines in the runs using the WSM6 and Morrison schemes start to catch up in intensity and development to the run using the Thompson scheme. Because the dominant size of graupel particles in the runs using the WSM6 and Morrison schemes is smaller, these particles take more time to fall below the freezing level and enhance the rainwater production and its evaporative cooling. In the run using the Thompson scheme, the graupel production slows down at later times while the snow particle growth increases, leading to more snow falling below the freezing level to melt and surpass graupel particle melting in the production of rainwater.

1. Introduction

Bulk microphysics schemes (BMSs) are commonly used in numerical weather/climate models to simulate the transport, physical change, and thermodynamic effects of the total hydrometeor population in clouds, in either liquid or frozen form or a mixture of both. Regardless of the degree of complexity, the role of a BMS is to simulate the population dynamics of hydrometeor particles as a response to the resolved air motion, and the feedback to the environment based on the behavior of individual hydrometeor particles (Wang 2013, Chapter 11). Hydrometeors in a BMS are described by one or more physical characteristics of the particles (such as mass mixing ratio and number concentration), and their population dynamics are governed by a transport equation with local source and sink terms. This transport equation is derived from a spectral balance equation for the hydrometeor size distribution function using the method of moments (Beheng 2010). A single-moment (1M) scheme includes prognostic equations for the mass mixing ratio, while a multimoment scheme will have prognostic equations for multiple characteristics that define the hydrometeor population (such as the number concentration or number mixing ratio).

Multiple BMSs with different levels of complexity are available in the Weather Research and Forecasting (WRF) Model (Skamarock et al. 2008), a community model widely used for research and operational forecasting needs. The complexity of these schemes varies in formulations from single moment (e.g., WSM6, Hong et al. 2004) to two moment (2M, e.g., Milbrandt and Yau 2005, Thompson et al. 2008 and Morrison et al. 2005 and 2009). These schemes have been evaluated and compared in simulations of various meteorological phenomena. Dudhia et al. (2008) were among the first to evaluate the BMSs in the WRF Model using sensitivity experiments for real cases of heavy precipitation.

Corresponding author: Jian-Wen Bao, jian-wen.bao@noaa.gov

DOI: 10.1175/MWR-D-18-0249.1

By modifying the WSM6 scheme so that both snow and graupel were treated as partially rimed particles with the same mass-weighted fall speed, they showed that the hydrometeor distributions in clouds and surface precipitation were affected. Van Weverberg et al. (2013) later examined the different behavior of one 1M and two 2M BMSs in a simulated tropical mesoscale convective system (MCS) using the WRF Model. They showed that the performance of the 2M schemes was not better than the 1M scheme in terms of simulated cloud and precipitation distributions and the simulated MCS was highly sensitive to the size- and density-dependent fallout rate of frozen hydrometeors. Han et al. (2013) conducted a similar study using the WRF Model and concluded that the Thompson scheme (a 2M scheme, Thompson et al. 2008) produced the best simulated radar reflectivity for a winter storm due to the scheme's better representation of hydrometeor size distributions, particularly for snow, compared to the other schemes.

Another way of evaluating different BMSs in the WRF Model is to use idealized simulations to compare different microphysics parameterization schemes on an equal footing in well-understood dynamical scenarios. Morrison et al. (2009) and Van Weverberg et al. (2012) both investigated the sensitivity of an idealized squall-line simulation to the representation of microphysics using BMSs in the WRF Model. These studies demonstrated that differences in the rain drop size distributions between the 1M and 2M schemes led to different rates of rainwater evaporation, produce different surface precipitation rates in the trailing stratiform region, and result in different intensity of cold pools behind the surface gust front. In a similar study, Bryan and Morrison (2012) showed that the use of the 2M schemes in the WRF Model overall improved the idealized squall-line simulation compared to observations by improving the overall rainwater evaporation which is critical to the squall-line development. They found that rain drop size distribution and the properties of rimed ice (either graupel or hail) in terms of density and fall speed were the two microphysical processes that affect the squall-line structure the most. Tao et al. (2016) provided a summary of important previous studies in which various BMSs were compared in the WRF Model, as well as in other convection-permitting numerical weather prediction models, in either idealized or real case studies. The foci of all these previous BMS comparison studies were on the response of the simulation to varying parameterization of microphysical processes and the relationships between hydrometeor size, mass and fall speed. In an idealized tropical cyclone simulation study, Bao et al. (2016) compared the differences in the process terms of the hydrometeor mass and number concentration tendency equations between a 1M and 2M BMS in an idealized case study of tropical cyclone development. They showed that the differences in the parameterized processes between the two schemes used in their study, which were related to the assumed hydrometeor characteristics such as mass-size distributions, led to the differences in the net diabatic heating associated with cloud and rain production and therefore in the development of the simulated tropical cyclone structure and intensity. These differences in the assumed hydrometeor characteristics highlight the large number of uncertainties in the spectral definition of individual hydrometeor categories and spectrum-dependent microphysical processes, and the fact that additional complexity in a scheme can lead to additional uncertainty. In a recent study, Xue et al. (2017) found that similar uncertainties exist in bin microphysics schemes.

This study uses simulations of an idealized 2D squall line, particularly during the developing phase, to analyze and compare individual microphysical process terms in the hydrometeor mixing ratio tendency equations, as well as the size characteristics of the simulated hydrometeor population, in three bulk microphysics schemes available in the WRF Model. The focus on the early stages of the squall-line development allows us to discern the differences in the parameterized processes that contribute to the divergence in solutions. According to Straka (2009), there are choices in how a specific microphysical process is parameterized because 1) different meteorological models practically require different levels of complexity in microphysics parameterizations, 2) it is difficult to develop theories and parameterizations that can cover the broadscale interaction in microphysical processes, and 3) there is no converged theory and observations to indicate what the exact form of the parameterization should be. On the other hand, no matter how complex a BMS is and how different from others in formulation, its output must include precipitation and microphysical characteristics of hydrometeor population, such as size distribution for all hydrometeors and the total mass of frozen hydrometeors. The purpose of this study is to use the comparison of the microphysical processes to gain a better understanding of the impact of the differences in the size distributions of hydrometeor population between these schemes on the development of an idealized 2D squall line. Due to the difficulty in measuring hydrometeor production rates associated with individual microphysical processes in nature, evaluating the performance of these schemes in terms of size distributions of hydrometeors and meteorological processes that are more readily observed may provide insight into the effectiveness of the schemes in simulating nature.

The rest of the paper is organized as the following. Section 2 provides an overview of the WRF Model setup and the three microphysics schemes to be compared. Section 3 presents the results from the idealized WRF simulations and the comparison of individual microphysical process terms in the mass mixing ratio tendency equations of hydrometeors for the three schemes. The summary and conclusions are given in section 4.

2. Overview of the WRF Model setup and the three microphysics schemes

The WRF Model version 3.7 (Skamarock et al. 2008) is used in this study with the configuration of the standard 2D idealized squall-line case. The 2D model domain covers 600 km horizontally at 1-km resolution with 80 model levels in the vertical direction. Following Morrison et al. (2009), all the simulations are initialized using the same initial and open boundary conditions, in which an environmental vertical wind shear in the lowest 2.5 km is prescribed to be $0.0048\,\mathrm{s}^{-1}$. A warm bubble with the maximum perturbation potential temperature of 3 K is prescribed at a height of 1.5 km to trigger the development of the simulated squall line. The perturbation potential temperature of the warm bubble tapers to zero following the cosine squared at the horizontal radius of 4 km and a vertical radius of 1.5 km. All the simulations are carried out for 6 h using a time step of 3 s. Output is written every minute, providing high time resolution for model analysis. Despite the fact that 2D idealized squall-line cases, such as the one used in this study, have been used for microphysics parameterization evaluation (see, e.g., Bryan and Morrison 2012), caution should be applied to interpreting the results from any 2D idealized simulation since the interaction between dynamics and microphysical processes in a 2D idealized squall line differs from that in simulations of a 3D real squall-line event.

Three microphysics schemes are compared in this study: the 1M WRF single-moment 6-class scheme (Hong and Lim 2006; the simulation using this scheme is referred to as the WSM6 run hereafter), the 2M scheme developed by Thompson et al. (2008) (the simulation using this scheme is referred to as the Thompson run hereafter), and the 2M scheme developed by Morrison et al. (2005 and 2009) (the simulation using this scheme is referred to as the Morrison run hereafter). The three schemes predict mass mixing ratios of cloud water, rainwater, cloud ice, snow, and graupel. The Thompson scheme predicts hydrometeor particle number mixing ratio for rainwater and cloud ice, while the Morrison scheme predicts the particle number mixing ratio for all the hydrometeors except for cloud water. Hydrometeor size distributions are assumed to be a generalized gamma function, and simple power laws are used to relate mass and fall speed to the size of each hydrometeor. The values for the coefficients used in the gamma functions and power laws for each scheme are summarized in Table 1. In the Morrison scheme, the coefficients used in the gamma function and power law for rimed ice can be set to either graupel or hail. In this study, the coefficients were set to graupel. It is important to note that the simulated size and mass distributions of hydrometeor populations in these schemes intrinsically depend not only on the size and density assumptions listed in Table 1, but also on the specific parameterizations of hydrometeor particle breakup, aggregation and size change through water phase-change processes (Straka 2009).

3. Results

a. *Dependence of the squall-line characteristics on microphysics parameterizations*

We first look at the dependence of the simulated structural characteristics of the idealized squall line on the different microphysics parameterization schemes. The simulated squall line develops mainly due to the cooling from evaporation and melting that is associated with hydrometeor fallout. The impact of this cooling on the structural development of the squall line has been well established (e.g., Weisman and Rotunno 2004). In the ensuing discussions, we define a squall line as the propagating gust front of a cold pool above the surface that is produced by the phase change of hydrometeors in convective clouds (mostly rainwater evaporation). We do not distinguish the morphology between a mature squall line and the prior gust front development and propagation. In all three simulations, moist convection starts within the first few minutes of the simulation as the initial warm bubble rises. As condensation occurs in the rising warm bubble, the release of latent heat intensifies the rising motion, which leads to the formation of cumulus/cumulonimbus clouds. The development of the squall line is the classical one; that is, it is initiated by tilted updrafts in cumulus/cumulonimbus clouds and it is maintained by new convection that forms as the leading edge of the cold pool, which is commonly referred to as the gust front, advances. Cloud ice begins to form after 10 min and precipitation at the surface starts to accumulate after 20 min. The structural evolution of the simulated squall line during the 6 h of the simulation is depicted in Fig. 1 by the cross sections of wind vectors, equivalent potential temperature and potential temperature perturbation at 1, 2, 4, and 6 h into the simulations. Early in the simulations (at or before 30 min; not shown),

TABLE 1. Summary of hydrometeor size distributions in the WSM6, Thompson, and Morrison schemes. The x denotes the hydrometeor type (i.e., c, r, i, s, or g for cloud water, rainwater, cloud ice, snow, or graupel). Number distribution: $N_x = N_{0x}D_x^{P_x}\exp(-\lambda_x D_x)$, mass–dimensional distribution: $m_x(D) = a_{mx}D_x^{b_{mx}}$, and fall speed–dimensional distribution: $V(D) = a_{vx}D_x^{b_{vx}}\exp(-\gamma_x D)$. Monodisperse (MONO) and exponential (EXP) distributions denote the actual distributions used in the individual schemes as special cases of the generalized gamma distribution (GAM). Also, the actual shape parameters for number distributions, in particular the intercept (N_{0x}), are complicated and the reader should refer to the code of each scheme for the actual mathematical expression.

Scheme	Species	Assumed distribution	N_{0x} ($\mathrm{m^{-4}}$)	a_{mx} ($\mathrm{kg\,m^{-b_{mx}}}$)	b_{mx}	a_{vx} ($\mathrm{m\,s^{-1}\,m^{-b_{vx}}}$)	b_{vx}	ρ_x ($\mathrm{kg\,m^{-3}}$)	γ_x	P_x
WSM6	Cloud	MONO	Varying to maintain a constant total number concentration of 300×10^6 ($\mathrm{m^{-3}}$)	$\pi\rho_r/6$	3	—	—	1000	0.0	0.0
	Rain	EXP	8×10^6	$\pi\rho_r/6$	3	841.9	0.8	1000	0.0	0.0
	Snow	EXP	Temperature dependent (Houze et al. 1979)	$\pi\rho_s/6$	3	11.72	0.41	100	0.0	0.0
	Graupel	EXP	4×10^6	$\pi\rho_g/6$	3	330	0.8	500	0.0	0.0
	Ice[a]	EXP	—	—	—	—	—	—	—	—
THOM	Cloud	GAM	100×10^6	$\pi\rho_c/6$	3	0.0	0.0	1000	195.0	Min (15, $10^9/N_{0c} + 2$)
	Rain	EXP	Prognostic	$\pi\rho_r/6$	3	4854.0	1	1000	195.0	0.0
	Ice	EXP	Prognostic	$\pi\rho_i/6$	3	1847.5	1	890	0.0	0.0
	Snow	EXP+GAM	Temperature dependent (Field et al. 2005)	0.069	2	40	0.55	Varying reciprocally with D[b]	100.0	0.636
	Graupel	EXP	Varying according to an assumed function of the total mass and size distribution parameters	$\pi\rho_g/6$	3	442	0.89	500	0.0	0.0
MORR	Cloud	GAM	Varying to maintain a constant total number concentration of 250×10^6 ($\mathrm{m^{-3}}$)	$\pi\rho_c/6$	3	3×10^7	2	997	0	Dependent on the droplet number concentration following observations (see Morrison et al. 2009)
	Rain	EXP	Prognostic	$\pi\rho_r/6$	3	841.99667	0.8	997	0	0
	Ice	EXP	Prognostic	$\pi\rho_i/6$	3	700	1	500	0	0
	Snow	EXP	Prognostic	$\pi\rho_s/6$	3	11.72	0.41	100	0	0
	Graupel	EXP	Prognostic	$\pi\rho_g/6$	3	19.3	0.37	400	0	0

[a] The distribution functions for cloud ice in the WSM6 scheme are significantly different from the Thompson scheme. In the WSM6 scheme, the total number mixing ratio of cloud ice is expressed as a function of cloud ice mixing ratio q_i, given by $N_i = c(\rho_{\mathrm{air}}q_i)^d$, where c and d are constants. The mass-weighted fall speed V_i is expressed similarly.

[b] The mass–size distribution in the Thompson scheme is assumed to be $m(D) = 0.069D^2$. Thus, if snow particles are spherical in the Thompson scheme, their density can be expressed as $0.414/(\pi D)$.

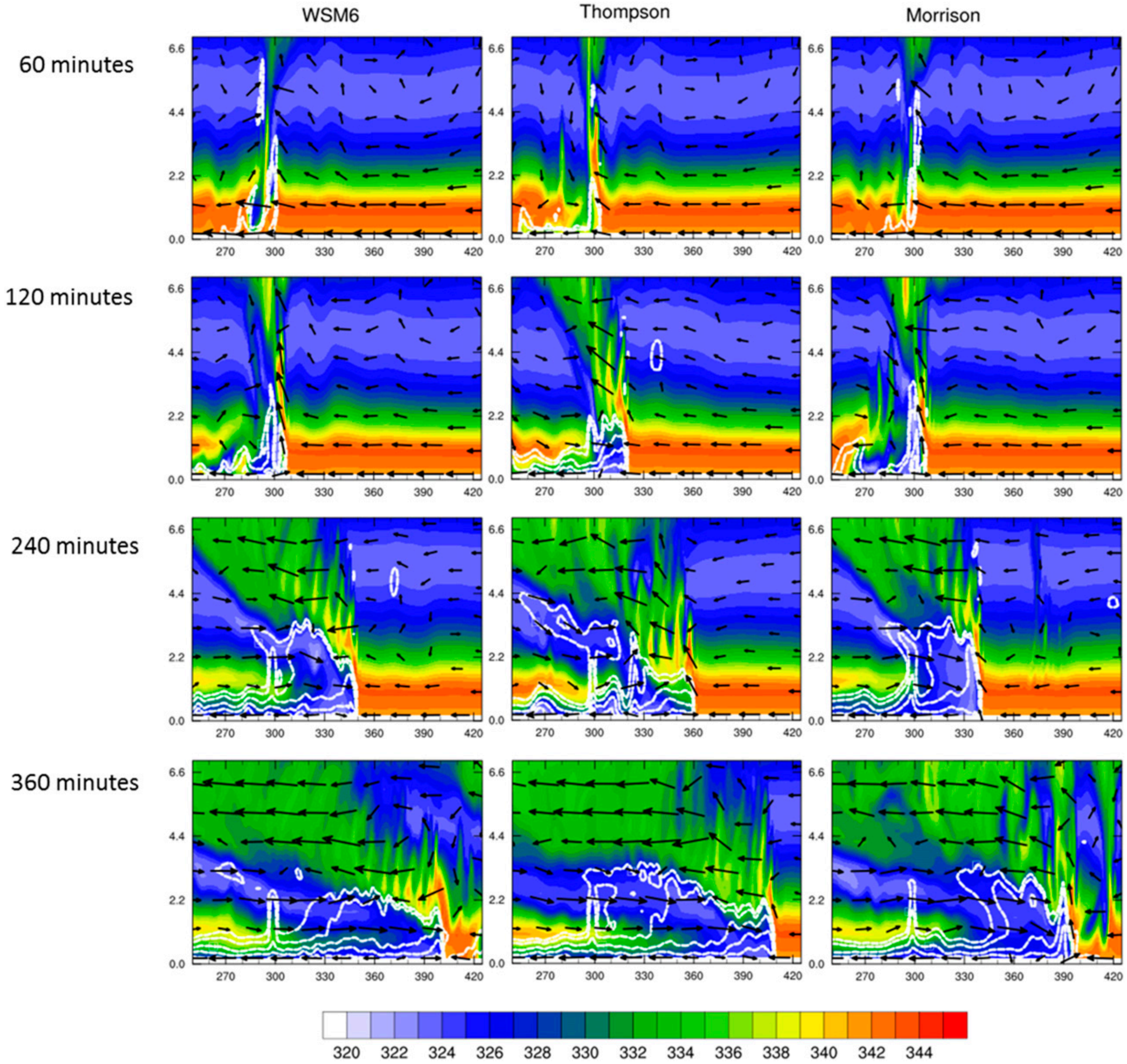

FIG. 1. 2D cross section of equivalent potential temperature (color shaded in K), potential temperature perturbation (dashed white lines, contour interval of 2 K beginning with −1 K), along cross-sectional winds, at (top row) 60 min, (second row) 120 min, (third row) 240 min, (bottom row) and 360 min into the simulations. (left) WSM6 run, (middle) Thompson run, and (right) Morrison run.

the simulated convection is upright or tilted slightly downshear in all three simulations. By 1 h into the simulation, the convection in the Thompson run becomes upshear tilted, while the convection in both the WSM6 and the Morrison runs is downshear tilted (as indicated by the distribution of equivalent potential temperature between 1 and 2 km above the surface). The transition to upshear tilted convection in the WSM6 and Morrison runs occurs after 90 min (not shown). By 2 h, the convection is upshear tilted and rear inflow has developed in all three runs. The gust front in the Thompson run is stronger (in terms of temperature perturbation behind the gust front) and faster propagating than in the other two runs. The intensity and propagation speed of the gust front are quite similar between the WSM6 and Morrison runs. These cross sections show that the dependence of the simulated structural evolution on the convection is consistent with previous conceptual models of squall-line evolution (Weisman et al. 1988; Lafore and Moncrieff 1989; Biggerstaff and Houze 1991, 1993). That is, in this 2D idealized case, when the cold pool is weak, the convection is upright or downshear tilted. When the cold pool becomes strong, the convection becomes upshear tilted. After 2 h of the simulations, the squall lines in the

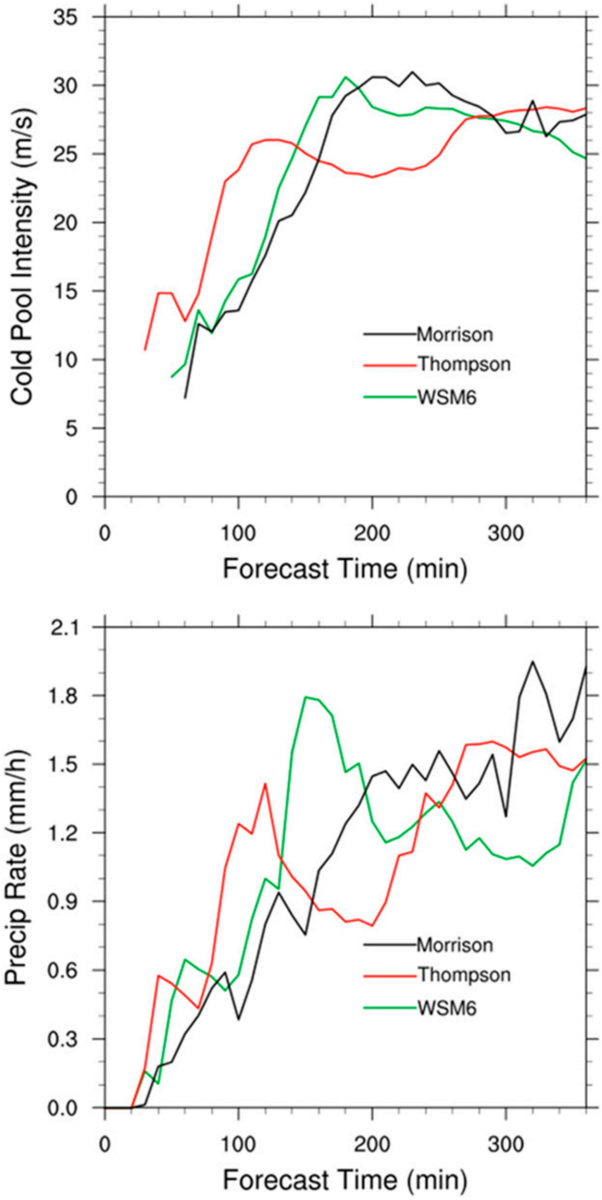

FIG. 2. Time series of (top) cold pool intensity and (bottom) precipitation rate averaged over the entire domain every 10 min. The green line is from the WSM6 run, the red line is from the Thompson run, and the black line is from the Morrison run.

WSM6 and Morrison runs that are less intense in the first 2 h start to catch up in intensity and development to the Thompson run.

Figure 2 summarizes the differences in the simulated squall-line structure in terms of cold pool intensity, widely used to depict the intensity and propagation speed of squall lines (see, e.g., Bryan and Morrison 2012, and Fan et al. 2017), along with the 10-min precipitation rate of the entire simulation domain. During the first 2 h, the Thompson run shows a faster increase in both squall-line intensity and precipitation rate than the other schemes. Since the same idealized environment is prescribed for all the simulations, the different cold pool intensities and precipitation rates depicted in Fig. 2 can only be attributed to the different microphysics parameterizations and the feedback to dynamics. In fact, as will be shown later in the analysis and comparison of various hydrometeor production rates, the differences in the simulated cold pool intensity are due to the differences in the size distributions and the size-dependent pathways of hydrometer production. Ultimately, these differences lead to differences in the strength of the cold pool and in the structural development of the simulated squall line as well as in the precipitation rate.

b. *Microphysical comparison of warm rain processes in the first 2 h*

The parameterized microphysical processes are all those terms on the right hand side of the hydrometeor tendency equations (see Table 2) that represent physical sources and sinks as well as redistribution via sedimentation. They can be grouped into those responsible for the interaction and evolution of liquid hydrometeors and those responsible for the production and loss of frozen hydrometeors, commonly referred to as warm rain processes and cold rain processes, respectively. As mentioned earlier, the development of the idealized squall line undergoes stages of warm bubble rising, cumulus/cumulonimbus formation, and organization of vigorous updraft and downdraft circulations. Only warm processes are present during the warm bubble rising and early cumulus formation, before the convection becomes deeper than the freezing level to involve cold rain processes. Therefore, to begin to understand the differences between schemes, we first examine the processes in the tendency equation of cloud water mass mixing ratio when only warm rain processes are present.

Saturation adjustment, in which supersaturation with respect to water is adjusted to zero when it occurs, is used to produce cloud water in all the schemes investigated in this study. The total number mixing ratio of cloud droplets is calculated using a prescribed gamma distribution (for the Thompson and Morrison schemes) and the mass of cloud water (see Table 1). Figure 3 shows all the process terms in the tendency equation of cloud water mass mixing ratio averaged over grid points 250–360 at 6 min into the simulation. Since no frozen processes are initiated by this time, condensation is the dominant process in all three simulations and the average cloud water profiles are very similar. This result indicates that the production rates of cloud water due to saturation adjustment are numerically very close to each other between the schemes. However, since the gamma

TABLE 2. The mass mixing ratio tendencies of cloud water (QCTEN), rainwater (QRTEN), ice (QITEN), snow (QSTEN), and graupel (QGTEN). The numbers in parentheses correspond to the numbers in the legends of Figs. 3–5, 8, 10, 12, 15, and 16. The sign (+/−) of the term corresponds to that used in the calculation of the budgets.

WSM6	Thompson	Morrison
QCTEN (1) =	QCTEN (1) =	QCTEN (1) =
− Homogeneous freezing (2)	− Homogeneous freezing (2)	+ Sedimentation (2)
− 2× average collection by snow and graupel (3)	− Collection by graupel (3)	+ Subsaturation adjustment (3)
− Collection by rain (4)	− Collection by snow to form graupel (4)	− Collection by rain (11)
− Heterogeneous freezing (5)	− Collection by snow to form snow (5)	− Autoconversion to rain (12)
− Autoconversion to rain (6)	− Collection by rain (6)	+ Homogeneous freezing (13)
+ Melting of cloud ice (7)	− Heterogeneous freezing (7)	+ Condensation/evaporation (14)
+ Condensation/evaporation (8)	− Autoconversion to rain (8)	If $T < 0^\circ$C:
	+ Melting of cloud ice (9)	− Collection by graupel (4)
	+ Condensation/Evaporation (10)	− Riming onto graupel/splintering to form ice (5)
		− Riming onto snow/splintering to form ice (6)
		− Collection by ice to form ice (7)
		− Heterogeneous freezing (8)
		− Collection by snow to form graupel (9)
		− Collection by snow to form snow (10)
QRTEN (1) =	QRTEN (1) =	QRTEN (1) =
+ Sedimentation (5)	+ Sedimentation (2)	+ Subsaturation adjustment (2)
+ Evaporation (6)	− Evaporation (3)	+ Sedimentation (10)
− Freezing to form graupel (7)	− Freezing to form ice (4)	+ Evaporation (11)
− Melting of graupel (8)	− Freezing to form graupel (5)	+ Instantaneous melting/freezing (12)
− Melting of snow (9)	+ Melting of graupel (6)	+ Collection of cloud water (18)
+ Collection of cloud water (13)	+ Melting of snow (7)	+ Autoconversion of cloud water (19)
+ Autoconversion of cloud water (14)	− Collection of ice to form graupel (8)	If $T \geq 0^\circ$C:
If $T > 0^\circ$C:	+ Collection of graupel (9)	+ Melting of small graupel (8)
− Enhanced melting of graupel due to accretion of water (2)	+ Collection of snow (10)	+ Melting of small snow (9)
− Enhanced melting of snow due to accretion of water (3)	+ Collection of cloud water (11)	− Melting of graupel (13)
+ 2× average collection of cloud water by snow and graupel (4)	+ Autoconversion of cloud water (12)	− Melting of snow (14)
If $T \leq 0^\circ$C:		If $T < 0^\circ$C:
− Collection of ice (10)		− Riming onto graupel/splintering to form ice (3)
− Collection by graupel (11)		− Riming onto snow/splintering to form ice (4)
− Collection by snow (12)		− Freezing to form graupel (5)
		− Collection by snow to form graupel (6)
		− Ice–rain collision to form snow (7)
		− Ice–rain collision to form graupel (15)
		− Collection by graupel (16)
		− Collection by snow (17)
QITEN (1) =	QITEN (1) =	QITEN =
− Melting of cloud ice (2)	− Melting of cloud ice (2)	+ Subsaturation adjustment, initial (2)
+ Heterogeneous freezing of cloud water (3)	+ Heterogeneous freezing of cloud water (3)	+ Subsaturation adjustment, final (3)
+ Homogeneous freezing of cloud water (4)	+ Rainwater freezing (4)	− Conversion of large ice to snow (4)
+ Sedimentation (5)	+ Homogeneous freezing of cloud water (5)	+ Heterogeneous freezing of cloud water (5)

TABLE 2. (*Continued*)

WSM6	Thompson	Morrison
− Collection by graupel (6)	+ Splintering (6)	+ Splintering of rain rimed onto graupel, forming ice (6)
− Collection by rain (7)	+ Sedimentation (7)	+ Splintering of rain rimed onto snow, forming ice (7)
− Collection by snow (8)	− Collection by rain (8)	+ Splintering of cloud water rimed onto graupel, forming ice (8)
− Autoconversion to snow (9)	− Collection by snow (9)	+ Splintering of cloud water rimed onto snow, forming ice (9)
+ Deposition/sublimation (10)	− Autoconversion to snow (10)	+ Homogeneous freezing of cloud water (10)
+ Ice nucleation (11)	+ Deposition/sublimation (11)	+ Sedimentation (11)
	+ Ice nucleation (12)	+ Collection of cloud water to form ice (12)
		− Ice–rain collision to form snow (13)
		− Ice–rain collision to form graupel (14)
		− Collection by snow (15)
		− Autoconversion to snow (16)
		+ Sublimation (17) + deposition (18)
		+ Ice nucleation (19)
QSTEN (1) =	QSTEN (1) =	QSTEN (1) =
+ Sedimentation (2)	− Splintering (2)	+ Subsaturation adjustment (2)
+ Melting of snow (3)	+ Deposition/sublimation of ice (3)	+ Instantaneous melting/freezing (3)
+ Evaporation (4)	+ Sedimentation (4)	+ Conversion of large ice to snow (4)
+ Enhanced melting due to accretion of water (5)	− Melting of snow (5)	− Small snow melting (5)
− Collection of snow by rain (6)	+ Collection of snow by rain (6)	+ Sedimentation (7)
+ Average collection of cloud water by snow and graupel (7)	+ Collection of cloud water by snow (7)	If $T \geq 0$°C:
+ Collection of ice by snow (8)	+ Collection of ice by snow (8)	+ Melting of snow (8)
+ Deposition/sublimation (9)	+ Deposition/sublimation of snow (9)	+ Evaporation (9) − collection of rain by snow to form rain (10)
+ Autoconversion of ice to snow (10)	+ Autoconversion of ice (10)	If $T < 0$°C:
+ Collection of rain by snow (11)		+ Sublimation (6)
+ Collection of ice by rain (12)		+ Collection of rain by snow to form snow (10)
+ Collection of rain by ice (13)		+ Collection of cloud water by snow (11)
− Autoconversion of snow to graupel (14)		+ Collection of ice by snow (12)
		+ Deposition (13)
		+ Autoconversion (14)
		− Collection of snow by rain to form graupel (15)
		+ Ice–rain collision, ice converts to snow (16)
		+ Ice–rain collision, rain converts to snow (17)
QGTEN (1) =	QGTEN (1)	QGTEN (1) =
+ Sedimentation (15)	− Splintering (2)	+ Subsaturation adjustment (3)
If $T > 0$°C:	+ Collection of graupel by rain (3)	− Small graupel melting (4)
+ Enhanced melting due to accretion of water (2)	+ Collection of cloud water by graupel (4)	+ Instantaneous freezing (15)
+ Evaporation (3)	+ Collection of cloud water by snow (5)	+ Sedimentation (17)
+ Melting (14)	+ Collection of snow by rain (6)	If $T \geq 0$°C:
If $T \leq 0$°C:	+ Collection of ice by rain (7)	+ Evaporation of melting graupel when subsaturated (5)
+ Collection of rain by graupel (4)	+ Deposition/sublimation (8)	+ Melting (16)
+ Collection of cloud water by averaged snow + graupel (5)	+ Freezing of rain (9)	If $T < 0$°C:
+ Collection of ice by graupel (6)	− Melting (10)	+ Freezing of rain (2)
+ Collection of snow by rain (7)	+ Sedimentation (11)	+ Collection of rain by graupel (6)
+ Collection of rain by snow (8)		+ Collection of cloud water by snow (7)
+ Collection of ice by rain (9)		+ Collection of cloud water by graupel (8)

TABLE 2. (*Continued*)

WSM6	Thompson	Morrison
+ Collection of rain by ice (10)		+ Collection of rain by snow (9)
+ Autoconversion of snow to graupel (11)		+ Collection of snow by rain (10)
+ Deposition/sublimation (12)		+ Ice–rain collision, ice converts to graupel (11)
+ Freezing of rain (13)		+ Ice–rain collision, rain converts to graupel (12)
		+ Sublimation (13)
		+ Deposition (14)

distributions for cloud water are prescribed differently, the same mass production rates of cloud water do not lead to the same total number concentrations of cloud droplets between the schemes.

In principle, different total number concentrations of cloud droplets between the schemes will lead to different rates of cloud droplets growing into rain through autoconversion, the process through which cloud

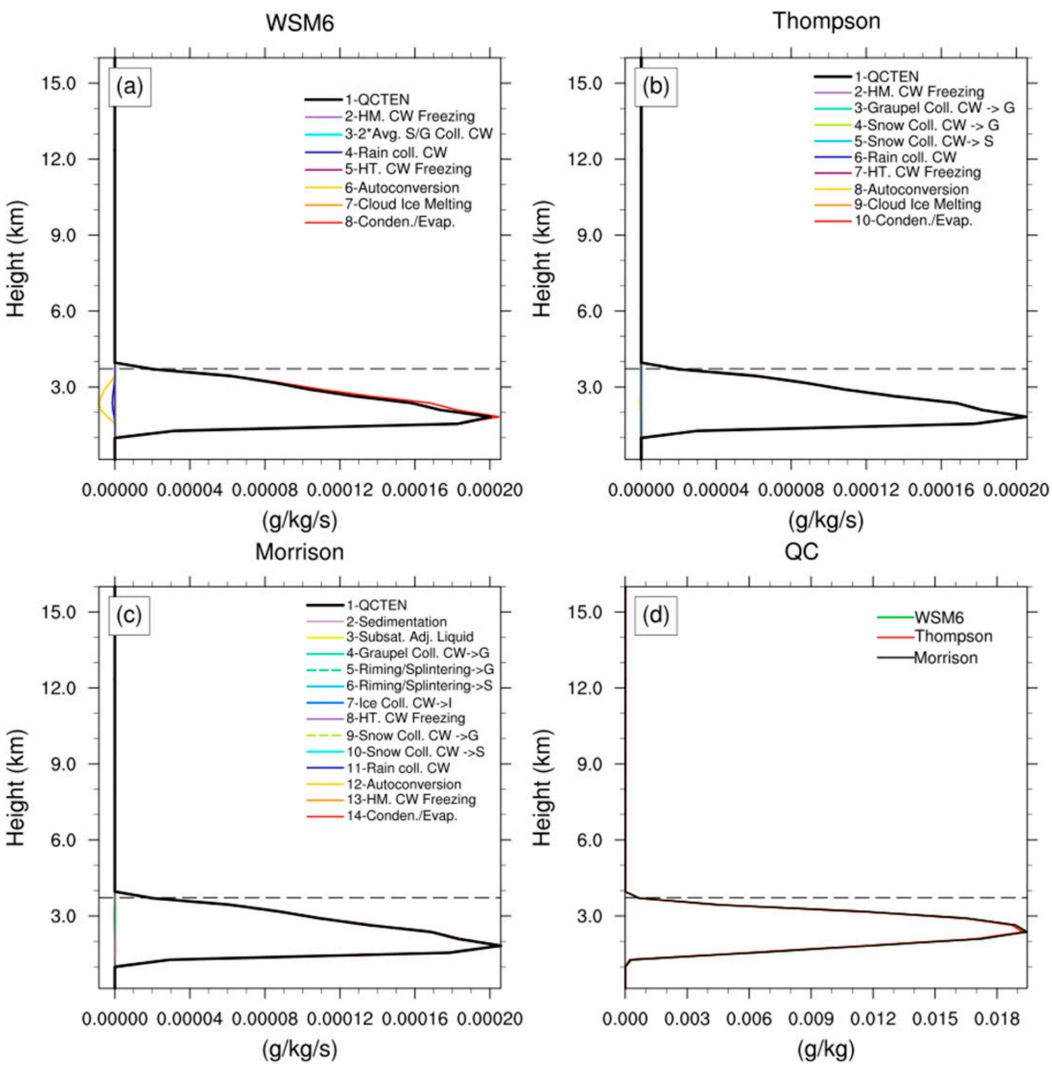

FIG. 3. The average vertical profiles of the process terms in the tendency equation of cloud water mass mixing ratio for the (a) WSM6, (b) Thompson, and (c) Morrison runs at 6 min into the simulations. (d) Cloud water mass mixing ratio from the three runs (the green line is the WSM6 run, the red line is the Thompson run, and the black line is the Morrison run). The black dashed line is the 0°C line. The legends are explained in Table 2. The average was done over the grid points 250–360.

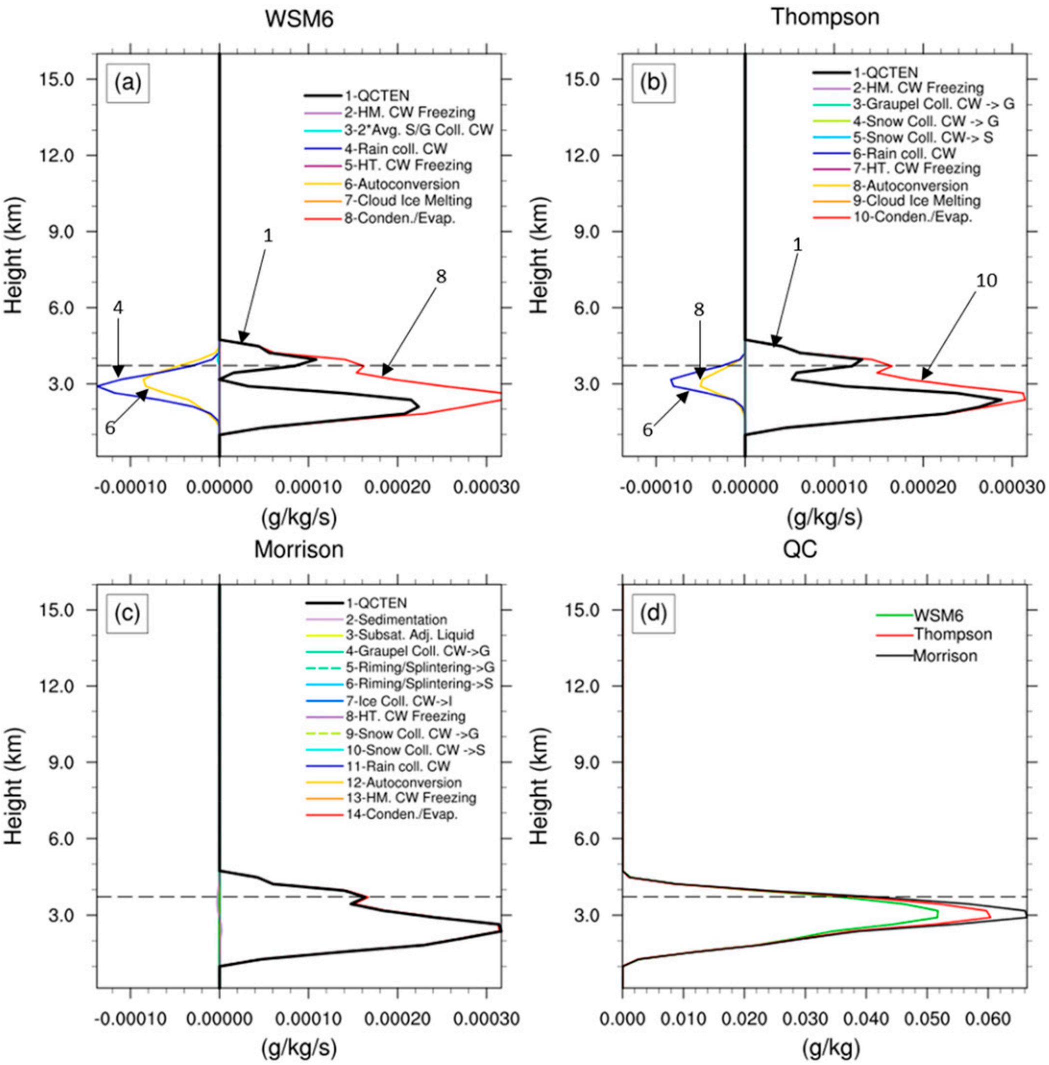

FIG. 4. The average vertical profiles of the process terms in the tendency equation of cloud water mass mixing ratio for the (a) WSM6, (b) Thompson, and (c) Morrison runs at 9 min into the simulations. (d) Cloud water mass mixing ratio from the three runs (the green line is the WSM6 run, the red line is the Thompson run, and the black line is the Morrison run). The black dashed line is the 0°C line. The legends are explained in Table 2. The average was done over the grid points 250–360.

droplets collide and coalesce with each other and grow in size to become rainwater particles. In addition to the difference in the total number concentrations of cloud droplets, the parameterization of autoconversion varies between the schemes not only due to different formulations, but also due to the different assumptions of the size distribution of rainwater particles in the fall speed specification (see Table 1). Consequently, the profiles of cloud mass mixing ratio will evolve differently between the runs. In fact, by 9 min into the simulation, differences in the cloud water mixing ratio begin to appear (Fig. 4). At this time, the Morrison run has the most cloud water, while the WSM6 run has the least (Fig. 4d) with all three runs showing a peak at about 3 km above the surface. Comparison of the process terms (Figs. 4a–c) indicates that, by this time, the magnitudes of the terms representing cloud water loss by autoconversion to rain and the collection of cloud water by rainwater are both smaller in the Thompson run than those in the WSM6 run, indicating more conversion of cloud water to rain in the WSM6 run compared to the Thompson run. In contrast, the magnitudes of all the process terms, except for condensation in the Morrison run, are negligible. These differences in the warm rain processes between the three runs lead to the production rates of frozen hydrometers that become so different after 20 min of the

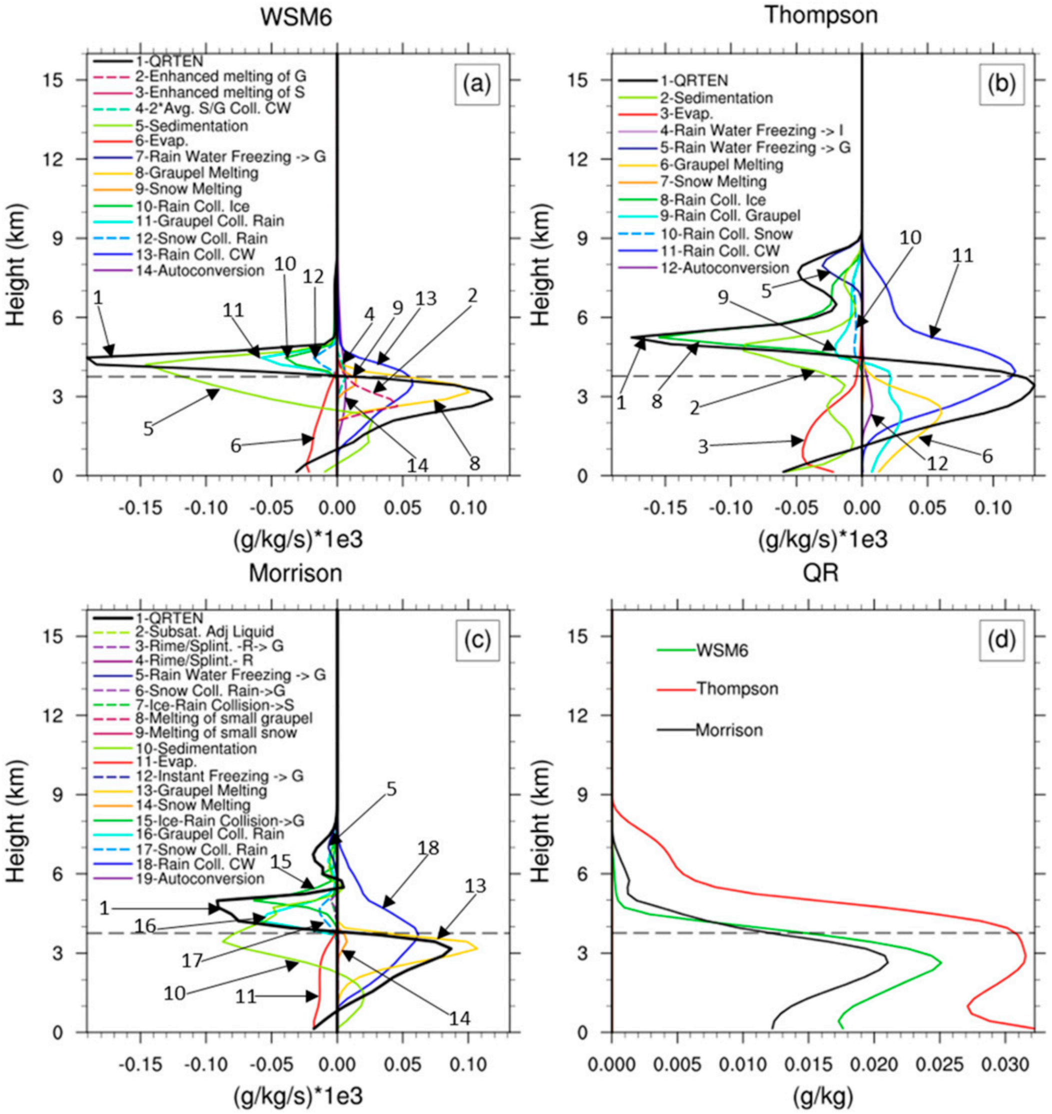

FIG. 5. The vertical profiles of the process terms in the tendency equation of rainwater mass mixing ratio for the (a) WSM6, (b) Thompson, and (c) Morrison runs averaged over the entire domain and during the first 2 h of the simulations. (d) Corresponding average rainwater mass mixing ratio from the three runs (the green line is the WSM6 run, the red line is the Thompson run, and the black line is the Morrison run). The black dashed line is the 0°C line. The legends are explained in Table 2.

simulations that the simulated convection starts to diverge in the distribution of vertical velocity as cold rain processes become more prominent (not shown).

To compare the relative importance of the microphysical process terms in forming rain during the early development of convection, vertical profiles of time- and area-averaged terms from the rainwater mixing ratio tendency equation are shown in Fig. 5 for the first 2 h of the simulations. The dominant pathways for rainwater production in the Thompson run are, in order of the maximum in the profile, rain collecting cloud water, graupel melting, rain collecting graupel and autoconversion. In the Morrison and WSM6 runs, rain collecting cloud water and graupel melting are similarly dominant. However, a small amount of melting snow also contributes to rainwater production in the WSM6 and Morrison runs during this time. The average vertical profiles in Fig. 5d indicate that during this time there are large differences in the rainwater mixing ratio. The process terms indicate that there is more rain collecting cloud water in the Thompson run above the freezing level than in the other two runs. Additionally, even though the magnitude of rainwater mass mixing ratio in the Thompson run is the greatest among the three above the freezing level, the magnitude of

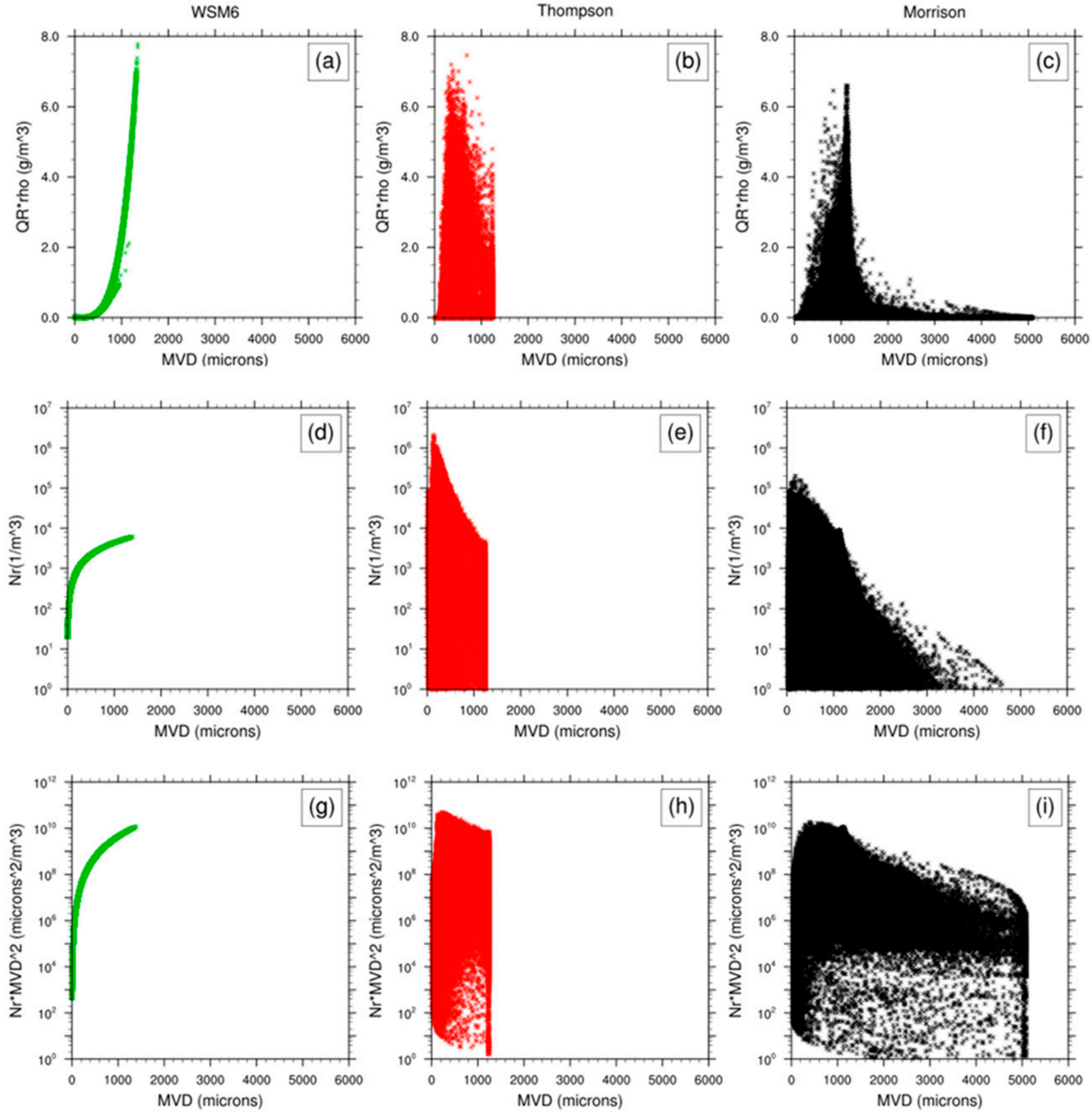

FIG. 6. The rainwater content vs mean volume diameter (MVD, μm) from the (a) WSM6, (b) Thompson, and (c) Morrison runs. The rainwater number concentration (m^{-3}) vs MVD (μm) from the (d) WSM6, (e) Thompson, and (f) Morrison runs. The effective total evaporation area vs MVD from the (g) WSM6, (h) Thompson, and (i) Morrison runs. Data points were sampled over the entire domain during the first 2 h of the simulations.

rainwater sedimentation is not, which together with more/stronger updrafts, makes the rainwater above the freezing level in the Thompson run stay aloft longer than in the other two runs. This is an indication that the size of the rainwater particles above the freezing level and their fall speed in the Thompson run are different than in the other runs. As will be seen in the later section on cold rain processes, the amount of supercooled liquid hydrometeors above the freezing level plays a significant role in the production rate of precipitating frozen hydrometeors in all three runs. Below the freezing level, the Thompson run also produces the most rainwater during this time. In the Thompson run, the peak of the graupel melting is close to 2 km, while graupel in the other two runs melts more quickly, resulting in a peak in the graupel melting term around the 3-km level.

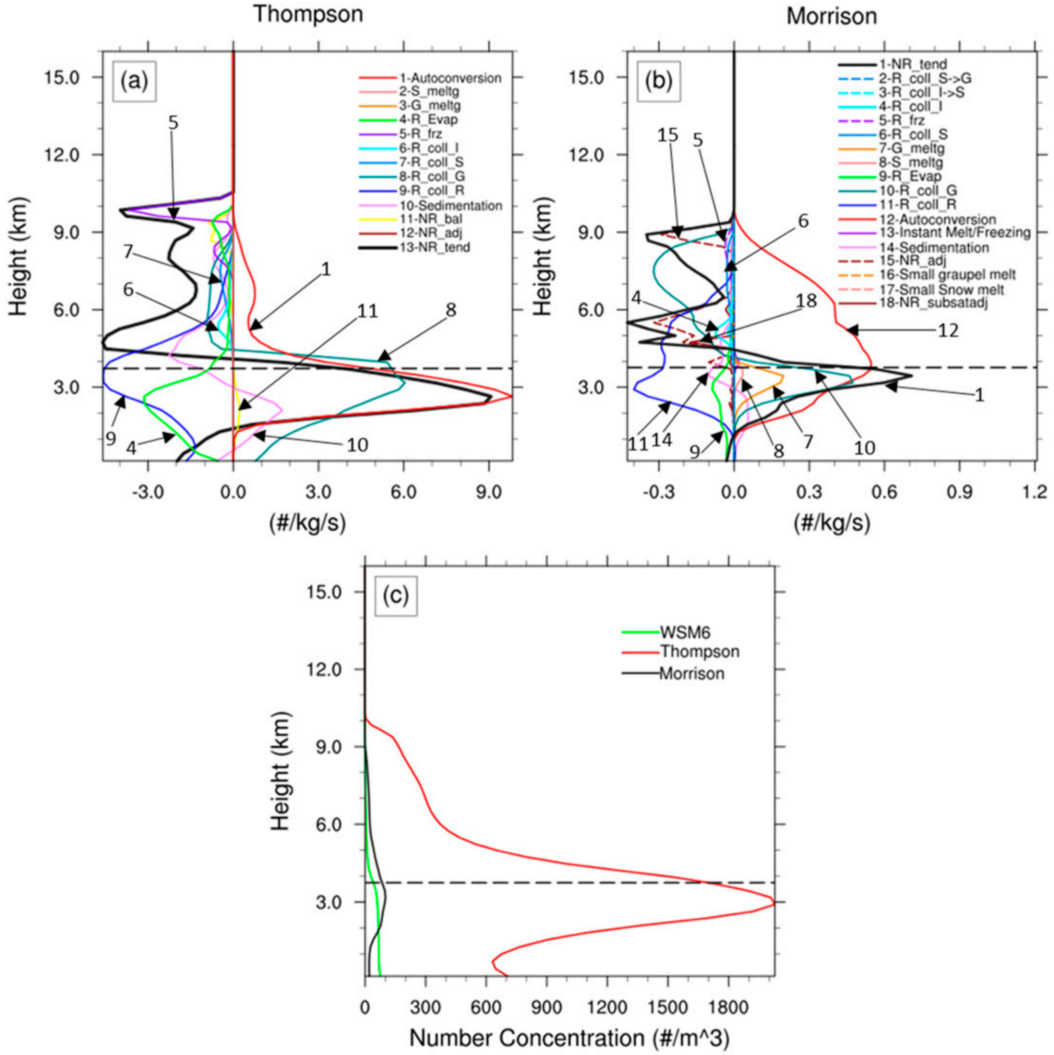

FIG. 7. The vertical profiles of the process terms in the tendency equation of rainwater number mixing ratio for the (a) Thompson and (b) Morrison runs averaged over the entire domain and during the first 2 h of the simulations. (c) Corresponding average vertical profiles of number concentration. The legends are explained in Table 3. The black dashed line is the 0°C line.

This difference points out that the size of the graupel in the Thompson scheme is significantly different than in the other two schemes, as will be shown later. The most prominent physical reduction terms of rainwater are freezing due to collision with frozen hydrometeors above the freezing level and evaporation below the freezing level in all three runs, with the overall evaporation term being greater in the Thompson run than the other two runs.

The higher evaporation rates and differing sedimentation rates seen in Fig. 5 for the Thompson run suggest that the raindrops in this scheme may have a smaller mean size. To compare the raindrop size distributions of the three schemes, Figs. 6a–c show the rainwater content versus mean volume diameter (MVD). In addition, the particle number concentration of rainwater (Figs. 6d–f) and the effective total evaporation area (Figs. 6g–i) versus MVD over the same area and time period as in Fig. 5 are shown. Figures 6a–c show that the Thompson run has rainwater particles with much smaller MVD than the other two runs. The MVD of rainwater particles increases with mixing ratio in the WSM6 run, which as a 1M scheme is not capable of allowing the spread of drop sizes that is seen in the Thompson and Morrison runs. The size distribution in the Thompson run is limited to below 1250 μm (in diameter) due to the upper bound imposed on the size of rainwater particles in terms of a median-volume diameter of 2.5 mm in the scheme. Figure 6 shows that there are many rainwater particles in the Morrison run that have MVDs larger than the upper limit in the Thompson run. In all three runs, most of the rainwater particles are smaller than 1250 μm.

The effective total evaporative area is defined as the multiplication of the square of the MVD and the particle number concentration. For a unit mass of rainwater, the smaller drops in the Thompson run will have a greater surface area to volume ratio, leading to more evaporation, and will fall more slowly, allowing more time to evaporate (Figs. 6g–i), which is consistent with the greater evaporation term shown in Fig. 5. Greater evaporation favors the formation of a more intense cold pool behind the gust front. This is one reason why the Thompson run results in a faster propagating squall line than the other two runs during the first 2 h of the simulation. It is important to point out that the differences in the size distributions of rainwater particles result from quantitative differences in the population dynamics that govern the evolution of rainwater particles between the schemes. These differences are not only determined by the assumed rainwater particle characteristics summarized in Table 1, but also due to the differences in individual parameterizations of hydrometeor particle gain/loss and modification through breakup and aggregation between the schemes.

Another important factor determining drop size is the particle number concentration. For the same mass and density, a greater number of particles will lead to smaller drops. Figure 7 shows the process terms in the tendency equation of rainwater number mixing ratio (Nr) for the Thompson and Morrison runs, along with vertical profiles of Nr for the same temporal and areal average as in Fig. 5. (The legends for Fig. 7 are explained in Table 3.) Note that the scales in Figs. 7a and 7b are different in order to better see the individual processes, since the Morrison run has much lower number concentrations. Since the WSM6 scheme is single moment, the number concentration is determined by the mass mixing ratio, and the processes responsible for the change of rainwater number concentration are the same as those responsible for the mass mixing ratio change (Fig. 5a). The Thompson run produces a much larger rainwater number mixing ratio than either the Morrison or WSM6 runs, which is consistent with the smaller drops in the Thompson run shown in Fig. 6. Examination of the process terms indicates that in the Thompson run, the autoconversion term and the term associated with shedding of rainwater, which occurs when rainwater particles break up in the rain-collecting-graupel process, are the largest sources of number mixing ratio. The term associated with shedding of rainwater in the Morrison run is much less than in the Thompson run below the freezing level (note the scale difference of the horizontal axes in Figs. 7a and 7b), although it acts as a collection term and is a major contributor to the reduction of Nr above the freezing level. Also, because the rain drops are smaller in the Thompson run, the reduction of rainwater number mixing ratio by evaporation plays a significantly greater role than in the other runs due to smaller drops evaporating faster. The WSM6 run, on the other hand, intrinsically does not include an explicit shedding term, as it does not predict Nr. All these explain why there is more evaporation below 1 km in the Thompson run than in the other two

TABLE 3. The equations for the number mixing ratio tendencies of rainwater (NRTEN) for the Thompson and Morrison parameterizations. The numbers in parentheses correspond to the numbers in the legends of Fig. 7. The sign (+/−) of the term corresponds to that used in the calculation of the budgets, and terms having the same name may appear with opposite signs for the different schemes, as the calculation of the process may differ.

Thompson	Morrison
NRTEN (13) =	NRTEN (1) =
+ Autoconversion of cloud droplets (1)	+ Evaporation (9)
+ Melting of snow to form raindrops (2)	+ Rain collecting other raindrops (11)
+ Melting of graupel to form raindrops (3)	+ Autoconversion of cloud droplets (12)
− Evaporation (4)	+ Instantaneous melting/freezing (13)
− Freezing (5)	+ Sedimentation (14)
− Rain collecting ice (6)	+ Adjustment to constrain raindrops to be within the assumed size range (15)
− Rain collecting snow (7)	+ Melting of small graupel (16)
− Rain collecting graupel (8)	+ Melting of small snow (17)
− Rain collecting other raindrops (9)	+ Subsaturation adjustment (18)
+ Sedimentation (10)	If $T \geq 0$°C:
+ Balance term to constrain raindrops to be within the assumed size range (11)	− Melting of graupel (7)
+ Adjustment term to constrain raindrops to be within the assumed size range (12)	− Melting of snow (8)
	− Rain collecting graupel (results in shedding of rain drops) (10)
	If $T < 0$°C:
	− Collection of rain by snow to form graupel (2)
	− Ice–rain collision, rain converts to snow (3)
	− Ice–rain collision, rain converts to graupel (4)
	− Freezing (5)
	− Rain collecting snow (6)
	− Rain collecting graupel (10)

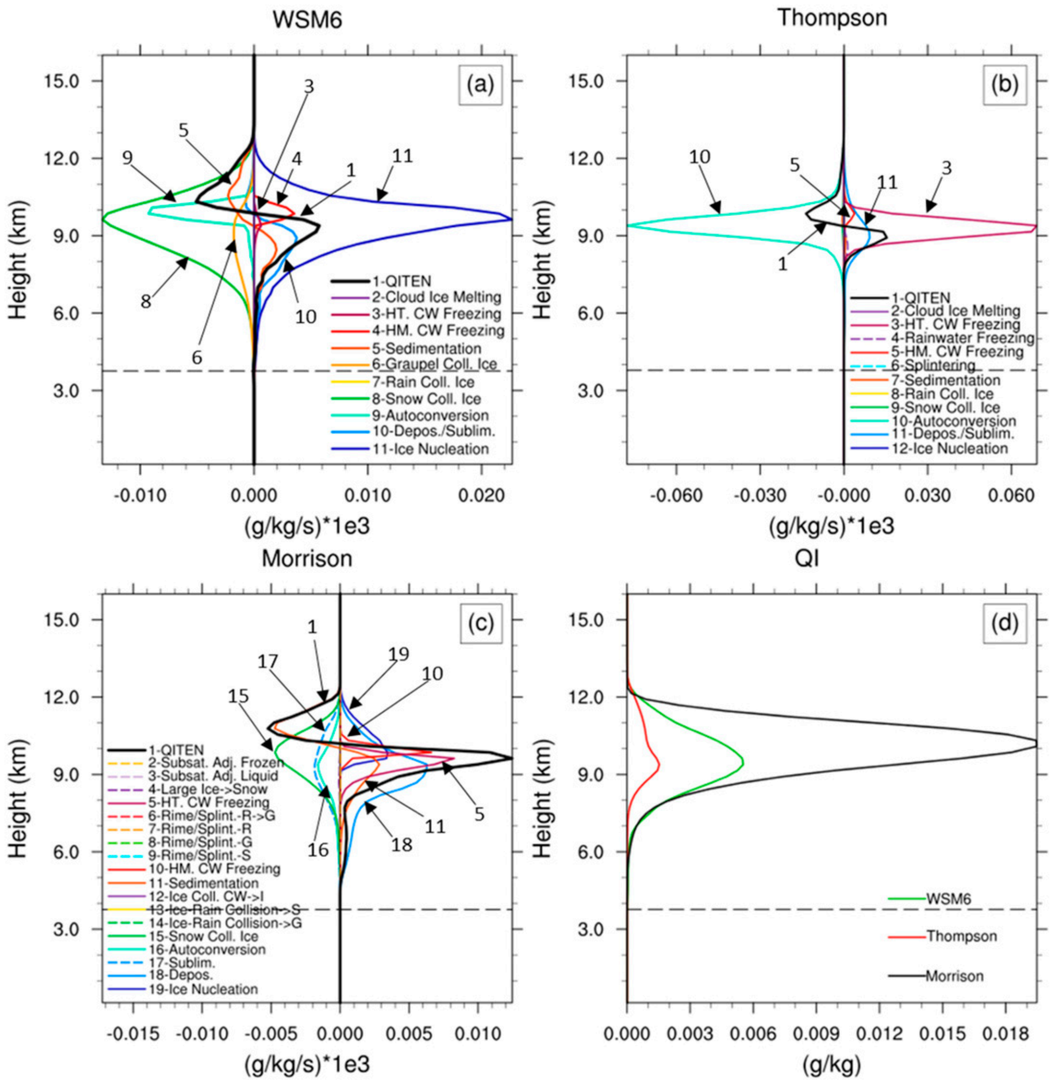

FIG. 8. The vertical profiles of the process terms in the tendency equation of cloud ice mass mixing ratio for the (a) WSM6, (b) Thompson, and (c) Morrison runs averaged over the entire domain and during the first 2 h of the simulations. (d) Corresponding average cloud ice mass mixing ratio from the three runs (the green line is the WSM6 run, the red line is the Thompson run, and the black line is the Morrison run). The black dashed line is the 0°C line. The legends are explained in Table 2.

runs during the first 2 h of the simulation, which is consistent with the stronger intensity and faster propagation speed of the squall line in the Thompson run during the same time.

This shedding term has a significant impact on the squall-line development. This can be seen by comparing our results to those of Fan et al. (2017) where the strength of the cold pool is less when using the Thompson scheme than when using the Morrison or WSM6 schemes. The version of the Thompson scheme used in our study includes the shedding of rainwater associated with rain collecting graupel in the Nr tendency equation when the temperature is warmer than 0°C, which was not included in the previous versions as was used in Fan et al. (2017). The small rain drops produced by the term enhance the cooling of the cold pool and therefore affect the propagation speed of the gust front. This explains most of differences between our results and those in Fan et al. (2017) regarding the intensity of the cold pool in the simulation using the Thompson scheme.

c. *Microphysical comparison of cold rain processes in the first 2 h*

The average vertical profiles of the process terms in the tendency equation of cloud ice mass mixing ratio

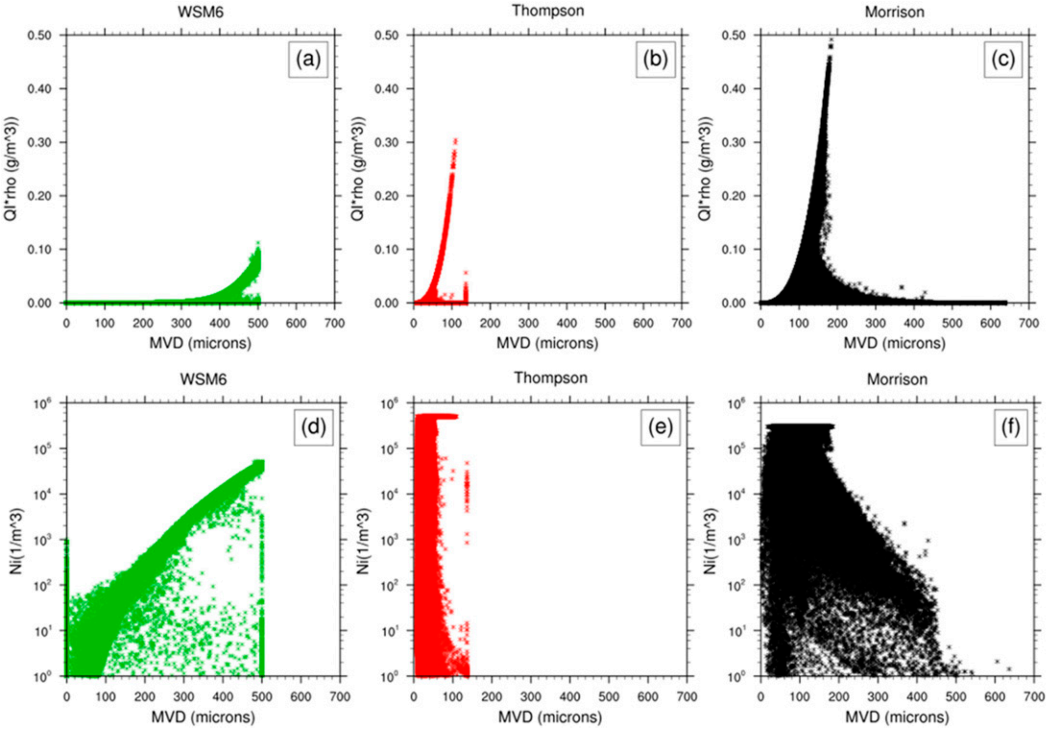

FIG. 9. The cloud ice content vs mean volume diameter (μm) from the (a) WSM6, (b) Thompson, and (c) Morrison runs. The cloud ice number concentration (m^{-3}) vs mean volume diameter (μm) from the (d) WSM6, (e) Thompson, and (f) Morrison runs. The data points were sampled over the entire domain and during the first 2 h of the simulations.

from the three runs are shown in Fig. 8 together with the average profiles of cloud ice mass mixing ratio (note that the *x* axes have different scales). These profiles are averaged over the entire domain as in Fig. 5. They indicate that the Morrison run produces by far the greatest net amount of cloud ice, while the Thompson run results in the least. The tendency equation of cloud ice mass mixing ratio for the WSM6 run includes production through ice nucleation, deposition and homogeneous freezing of cloud water. There is also a small amount of heterogeneous cloud water freezing. The main pathways to the reduction of cloud ice are through autoconversion of ice to snow, snow collecting ice, and graupel collecting ice. There is also a small amount of sublimation. In the Thompson run, the dominant pathways to cloud ice production are heterogeneous cloud water freezing, deposition and homogeneous cloud water freezing, while the dominant pathway to reduction is autoconversion to snow. The dominant pathways to cloud ice production in the Morrison run are ice nucleation, heterogeneous and homogeneous freezing of cloud water, and deposition, while the reduction pathways are collection of ice particles by snow, sublimation and autoconversion to snow. The different magnitudes of the dominant individual processes between the three runs not only strongly depend on the hydrometeor size distributions, but also significantly affect the size distribution and production not only of ice, but also of other hydrometeors as well, due to production and reduction terms that involve ice.

It is noteworthy that the major pathways for cloud ice production in terms of production rate are different between the three runs. There are three factors contributing to the differences. First, the three schemes differ in the assumed processes included in the calculation of the production and reduction of cloud ice, as is evident from the ice mixing ratio tendency equations provided in Table 2. Second, the relative magnitude of the same production/reduction terms differs. For example, there is significantly less autoconversion of cloud ice to snow in the Morrison run than in the other two runs. In addition, nucleation is a major contributor to cloud ice production in the WSM6 and Morrison runs, but not in the Thompson run. Third, the definition of ice versus snow in a model is based on an arbitrary size definition, and the three schemes each have their own size threshold for when frozen particles are considered large enough to be categorized as snow. The threshold size is 500 μm in the WSM6 code as the upper bound of the maximum dimension (called

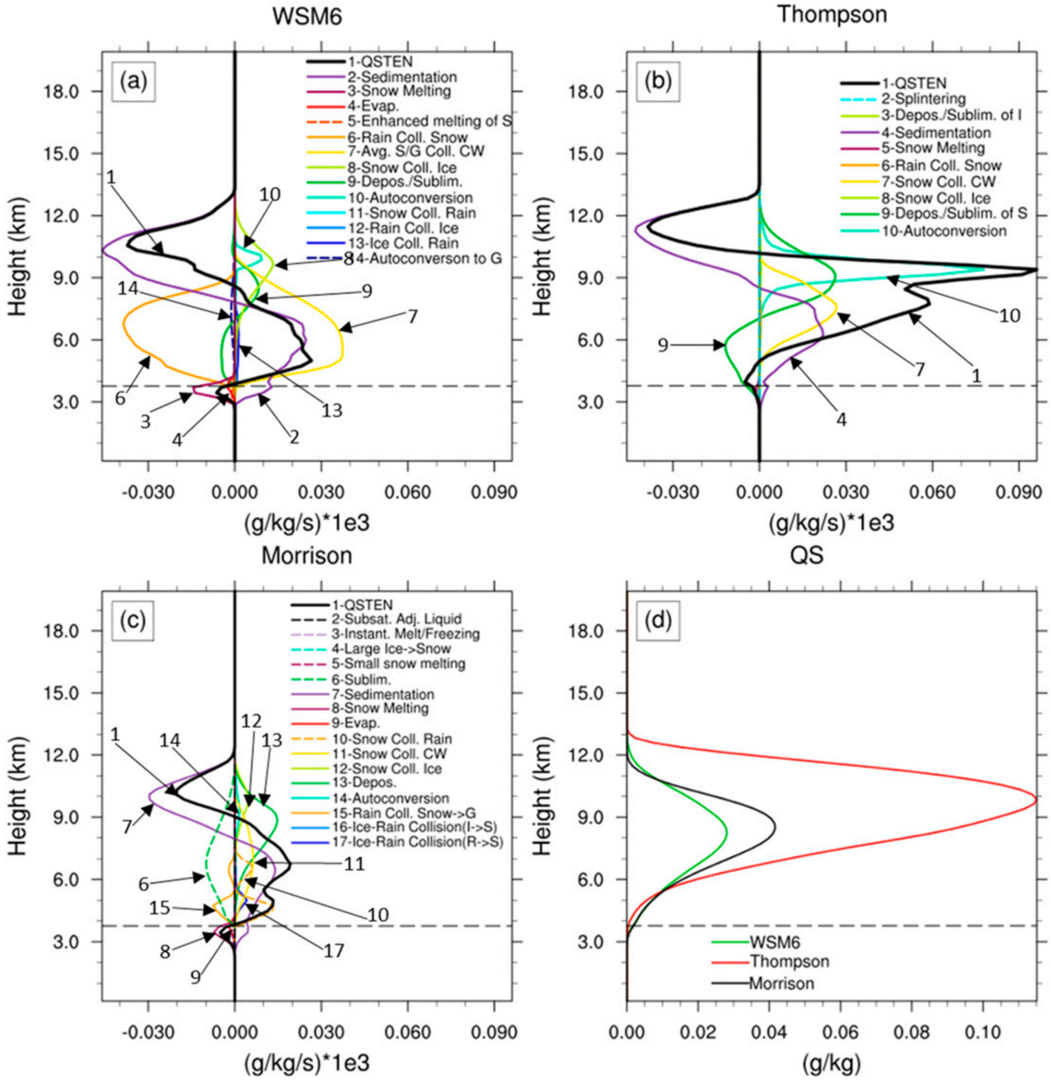

FIG. 10. The vertical profiles of the process terms in the tendency equation of snow mass mixing ratio for the (a) WSM6, (b) Thompson, and (c) Morrison runs averaged over the entire domain and during the first 2 h of the simulations. (d) Corresponding average snow mass mixing ratio from the three runs (the green line is the WSM6 run, the red line is the Thompson run, and the black line is the Morrison run). The black dashed line is the 0°C line. The legends are explained in Table 2.

diameter) of cloud ice particles in the calculation of mass and fall speed. In the code of the Thompson and Morrison schemes, it is set as the upper bound of the intercept parameter in the calculation of mass and fall speed such that the actual threshold sizes for the two schemes are about 150 and 650 μm, respectively. This prescribed size separator between ice and snow in all three schemes plays an important role in determining how much cloud ice is allowed to grow before it will be converted to snow, and consequently critically contributes to the different mass mixing ratio distributions of cloud ice and snow. Although these factors are about different details in the three microphysics schemes, there are no first physical principles and observations based on which we can discern which scheme has more accurate process parameterizations. This, in fact, reflects the general difficulty in the parameterization of hydrometeor conversion from one category to another.

This difference in the definition of cloud ice particle size is illustrated in Fig. 9, which shows the cloud ice content and the particle number concentration of cloud ice versus MVD over the same area and time period as in Fig. 8. For a given amount of cloud ice, the MVD of cloud ice particles in the WSM6 run is larger than in the Thompson and Morrison runs (Figs. 9a–c).

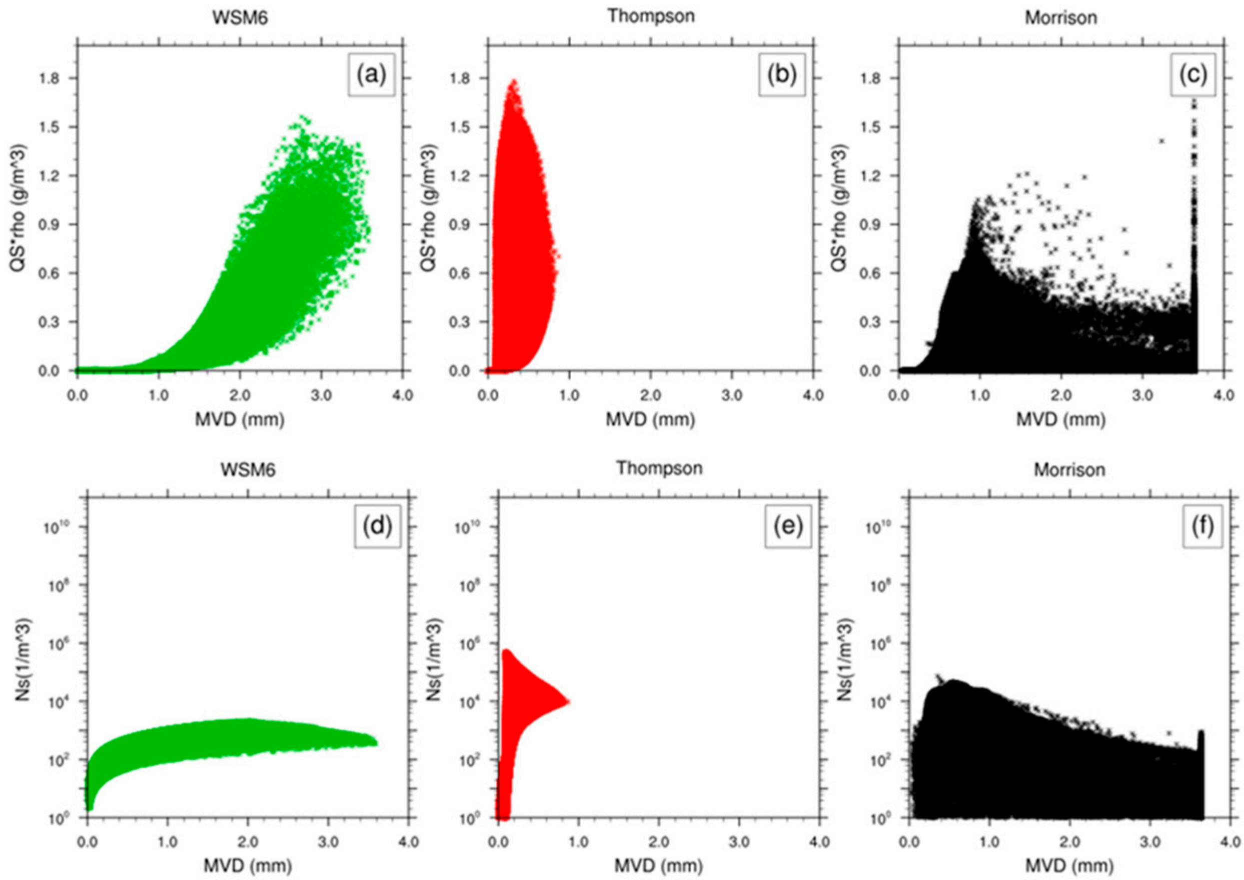

FIG. 11. The snow content vs mean volume diameter (mm) from the (a) WSM6, (b) Thompson, and (c) Morrison runs. The snow number concentration (m^{-3}) vs mean volume diameter (mm) from the (d) WSM6, (e) Thompson, and (f) Morrison runs. The data points were sampled over the entire domain and during the first 2 h of the simulations.

The Morrison run produces more mass and a greater range of the MVD of cloud ice than in the Thompson run. All these indicate that the dominant size of cloud ice particles (assumed to be bullet shaped) in the WSM6 run is greater than in the other two runs. Among the three runs, the cloud ice particles produced in the Thompson run are the smallest in size, while the total mass of cloud ice particles in the Morrison run is the greatest. From Figs. 9d–f, the Thompson run has a very large number of very small ice particles, while the WSM6 run has smaller number concentrations but ice particle sizes up to 500 μm. The Morrison run has a few ice particles that are even larger (up to 650 μm), but the majority of the ice particles are less than 200 μm. These differences in the size distribution of cloud ice between the schemes physically lead to differences in the snow and graupel production according to the microphysical mechanism between cloud ice and snow/graupel production (Straka 2009). Observations of cloud ice size distributions could be useful in resolving this difference in ice-snow definition.

There are also different pathways for snow production and reduction between the three runs. Figure 10 shows the vertical profiles of the various production terms in the snow mass mixing ratio tendency along with the snow mass mixing ratio, averaged over the same area and time period as Fig. 8. This figure shows that the Morrison and Thompson runs produce greater maxima in snow mass mixing ratio than the WSM6 run, with that of the Thompson run far exceeding the others. The snow production in the WSM6 run above 10 km is through autoconversion of cloud ice to snow and snow collecting cloud ice. Snow production below 10 km in the WSM6 run is due to the collection of cloud water by snow and graupel, deposition, snow collecting ice, and ice collecting rain. The major pathway for the reduction of snow in the WSM6 run is rain collecting snow to produce graupel. Additionally, there are contributions to the reduction of snow from sublimation and melting, but these processes are much smaller than the process of rain collecting snow. The major pathways of snow production in the Thompson run are

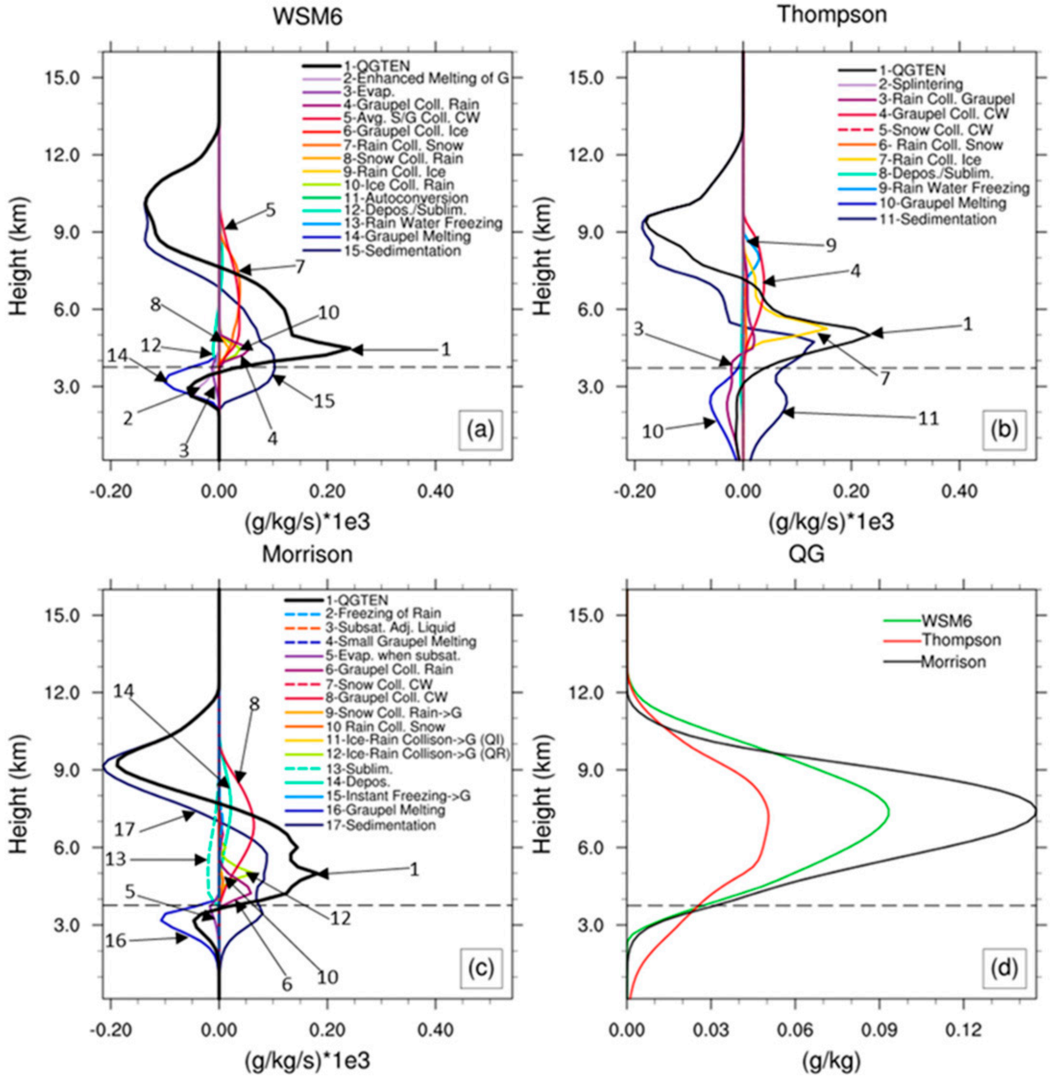

FIG. 12. The vertical profiles of the process terms in the tendency equation of graupel mass mixing ratio for the (a) WSM6, (b) Thompson, and (c) Morrison runs averaged over the entire domain and during the first 2 h of the simulations. (d) Corresponding average graupel mass mixing ratio from the three runs (the green line is the WSM6 run, the red line is the Thompson run, and the black line is the Morrison run). The black dashed line is the 0°C line. The legends are explained in Table 2.

autoconversion from ice, deposition, and snow collecting cloud water. Unlike the WSM6 run, sublimation is the most significant reduction pathway for snow in the Thompson run. Melting becomes more significant later in the Thompson simulation once more snow forms, although it is much smaller than sublimation during the entire simulation (not shown). The main pathways of snow production in the Morrison run during the same time period are snow deposition, autoconversion, snow collecting cloud water and ice, and closer to the freezing level, snow collecting rain and a small amount of ice-rain collisions. The pathways of reduction of snow for the Morrison run are sublimation of snow and closer to the freezing level, collection of snow by rain. Below the freezing level, the reduction processes are snow melting and evaporation. Like the other two runs, melting becomes more significant later in the simulation, but is much smaller than sublimation and rain collecting snow (not shown).

Figure 11 shows the mass content and the particle number concentration of snow versus MVD over the same area and time period as in Fig. 10. It should be noted that we use mass mean diameter of snow in the Thompson scheme to compare with MVD for the other two schemes (i.e., MVD is actually calculated as mass mean diameter for the Thompson scheme).

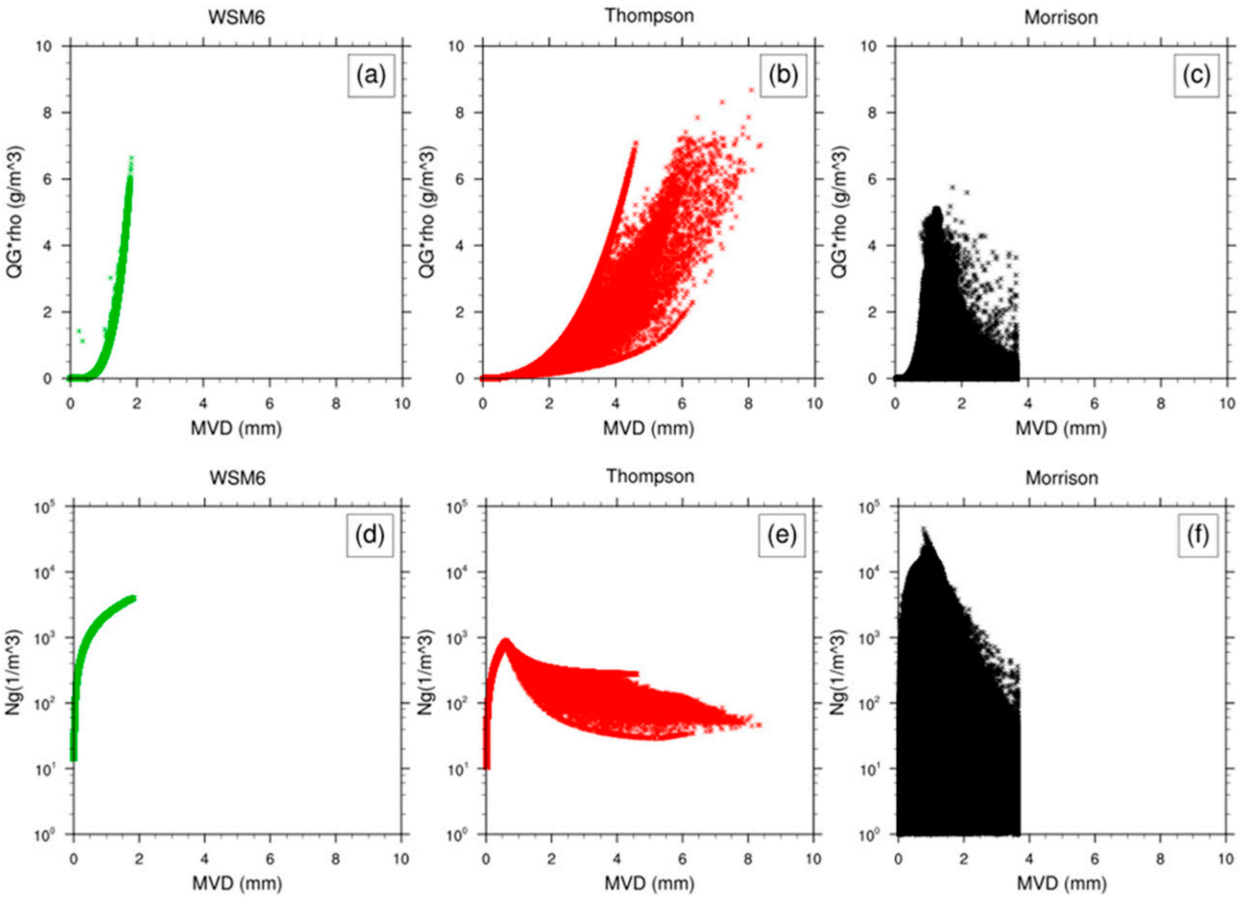

FIG. 13. The graupel mass content vs mean volume diameter (mm) from the (a) WSM6, (b) Thompson, and (c) Morrison runs. The graupel number concentration (m^{-3}) vs mean volume diameter (mm) from the (d) WSM6, (e) Thompson, and (f) Morrison runs. The data points were sampled over the entire domain and during the first 2 h of the simulations.

This is because the density of snow in the Thompson scheme is not constant with snow particle size. The size of snow particles in both the WSM6 and Morrison runs does not exceed 4.0 mm because of the limit placed on the slope parameter for snow in both schemes. In the Thompson run, the MVD of all the snow particles is less than 1 mm. Overall, there are many more snow particles of smaller sizes in both the Thompson and Morrison runs than in the WSM6 run (Figs. 11d–f). This size difference between the runs fundamentally results from the different assumptions in snow physical properties (size distribution parameters) and different size-dependent process parameterizations between individual schemes, despite the fact that the differences between the schemes lead to differences in dynamics which in turn feedback to the microphysical differences. These differences in the size distribution of snow particles have two consequences. First, they lead to different sedimentation rates for the same mass mixing ratio due to the differences in size-dependent fall speed. Second, they affect all the size-dependent microphysics processes contributing to the changes of the total snow content such as deposition/sublimation, collection and riming to form graupel. All these size-dependent differences in process parameterizations between the runs contribute to the differences in the production and reduction of rainwater from frozen hydrometeors, such as melting, which lead to the differences in the simulated development and strength of the squall line.

Figure 12 shows the vertical profiles of the graupel production terms and mass mixing ratio. Overall, the Morrison and WSM6 runs have the most graupel above 4 km, while the Thompson run has the least graupel aloft and most below the freezing level. The main pathways for the production of graupel in the WSM6 run are graupel and snow collecting cloud water, rain collecting snow, as well as collection of rain by ice, snow and graupel near the freezing level. In the Thompson run, the dominant pathways to graupel

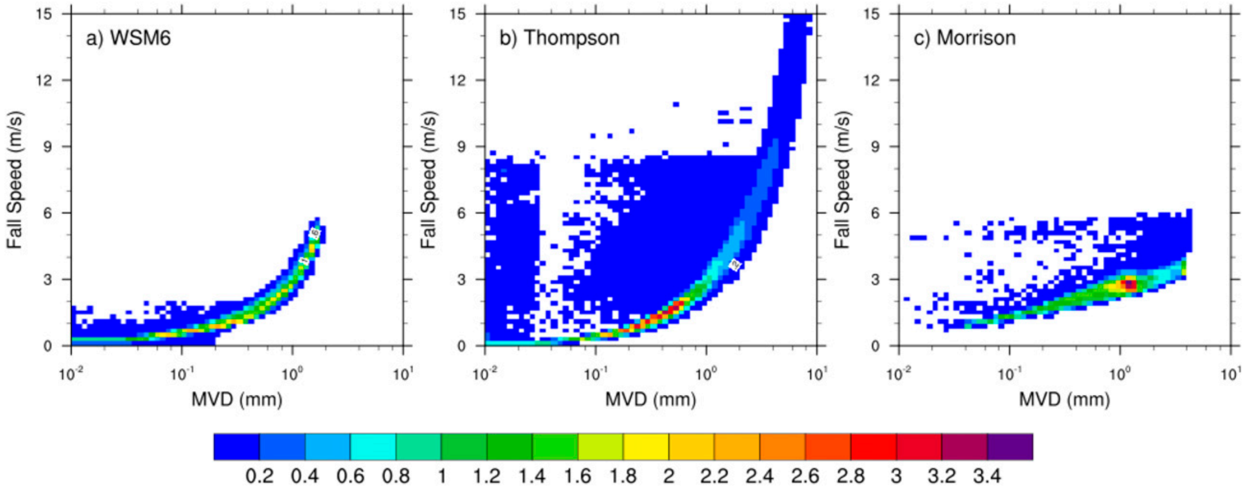

FIG. 14. Number of instances in which the mass-weighted fall speed of graupel and its mean volume diameter fall within a particular bin for the WSM6, Thompson, and Morrison microphysics schemes. At each output time, all points in the model domain with graupel content greater than 1.0×10^{-12} kg m^{-3} were included. For readability, the number count has been divided by 1000. Each panel shows the sum of all points in each bin during the first 2 h of the simulations, with output every minute.

production are collection of cloud water by graupel, freezing of rainwater, collection of cloud ice by supercooled raindrops, and rain collecting graupel. The dominant pathways to graupel production in the Morrison run are collection of cloud and rainwater by graupel, collection of snow by rainwater, deposition, and collection of cloud ice by supercooled raindrops. In all three runs, melting is the dominant reduction pathway for graupel. However, the Thompson run has a greater reduction pathway of rainwater collecting graupel and has more freezing of rainwater to form graupel than the other two runs.

One of the biggest differences in the contributing terms to the mass mixing ratio tendency equation of graupel between the three runs is in sedimentation below the freezing level. This is an indication that the size and the assumed density of the graupel are different between the schemes. Figure 13 shows the graupel mass content and number concentration versus MVD for the time period and area over which the profiles shown in Fig. 12 are averaged. It is clearly seen that the MVD for graupel is larger in the Thompson run than in either the WSM6 run or the Morrison run (Figs. 13a–c) and, overall, there are many more graupel particles of smaller sizes in both the Morrison and WSM6 runs than the Thompson run (Figs. 13d–f). Consistent with the differences in the density and fall speed parameters (see Table 1), as well as in riming growth of graupel between the schemes, graupel is bigger and falls faster in the Thompson run than in the other two runs during this time period. Figure 14 shows the frequency of the mass-weighted fall speed versus MVD for graupel during the first 2 h for the three runs, indicating that the Thompson run has significantly more graupel particles that are greater in size and fall faster than those in the other two runs. The mass-weighted fall speed was directly output from each run. Note that the fall speed that is plotted for the WSM6 run in Fig. 14a is actually a weighted average of the graupel and snowfall speeds since that is what is used in the code to calculate both graupel and snow sedimentation and collection terms. The comparison of sedimentation terms shown in Fig. 12 also confirms the larger size and faster fall speeds as the Thompson run has more sedimentation from 4 to 6 km, just above the freezing level. Consequently, the graupel in the Thompson run reaches the ground, as is seen in Fig. 12, while the graupel in the other two runs does not (in fact, in both the Morrison and WSM6 runs, graupel melts entirely before reaching the ground during the entire period of the simulation).

Overall, during the first 2 h of the simulations, the Thompson run, which has the smallest dominant size of rainwater particles but largest dominant size of graupel particles, produces the most intense squall line with the greatest propagation speed. With the greatest dominant size of rainwater particles, but smallest dominant size of graupel particles among the three runs, the WSM6 run results in the least amount of rainwater to evaporate which leads to the weakest squall line. This is because rainwater particles of smaller dominant size tend to evaporate faster, resulting in more cooling, leading to a stronger cold pool and faster squall-line propagation, while graupel particles of larger sizes lead to more rainwater production due to melting.

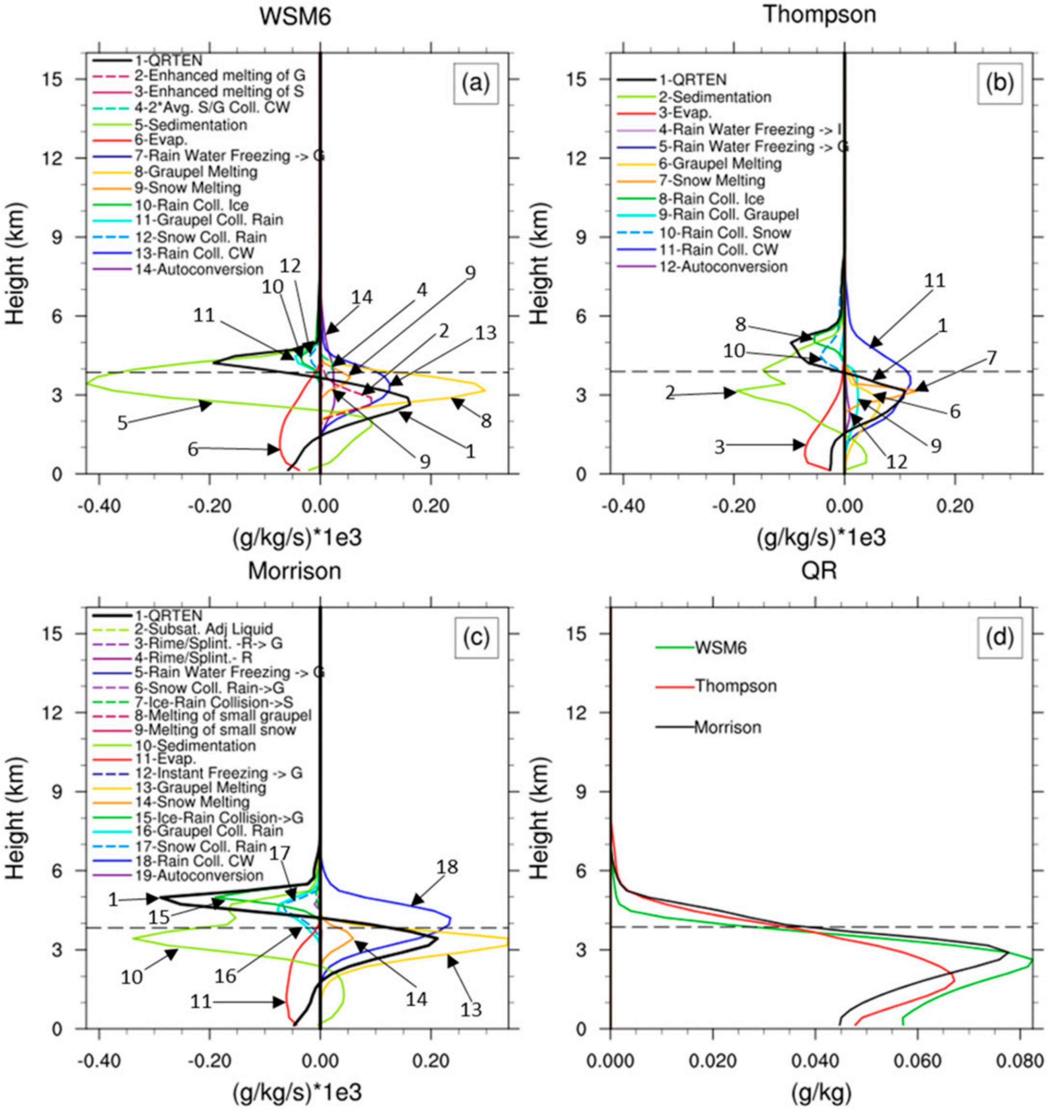

FIG. 15. As in Fig. 5, but averaged over 2–4 h of the simulations. The legends are explained in the Table 2.

d. *Comparison of prominent microphysical processes beyond 2 h*

As shown in Figs. 1 and 2, the simulated squall line continues evolving differently with the use of different BMSs after 2 h of the simulations. Although the cold pool intensity is due to cooling associated with both the melting and sublimation of frozen hydrometeors and the rainwater evaporation, the rainwater evaporation is in fact the most prominent, as will be shown in section 3e. Figures 15 and 16 show the vertical profiles of the domain-averaged process terms in the rainwater mass mixing ratio tendency equation and rainwater mass mixing ratio time averaged over 2–4 (Fig. 15) and 4–6 (Fig. 16) h of the simulations, for the purpose of illustrating the differences in the impact on the simulated squall line due to different size distributions and the size-dependent process parameterizations between the three BMSs. Comparing to Fig. 5, the maxima of rainwater evaporation rates in the WSM6 and Morrison runs increase to the point at which they are much more similar to that of the Thompson run between 2 and 4 h of the simulations. This is due to the snow and graupel particles of smaller dominant size in the WSM6 and Morrison runs falling below the freezing level and melting, enhancing the rainwater production and therefore evaporation. It is also interesting that the evaporation rates in the WSM6 and Morrison runs between 2 km and the freezing level are greater than in the Thompson run during this time. The enhanced

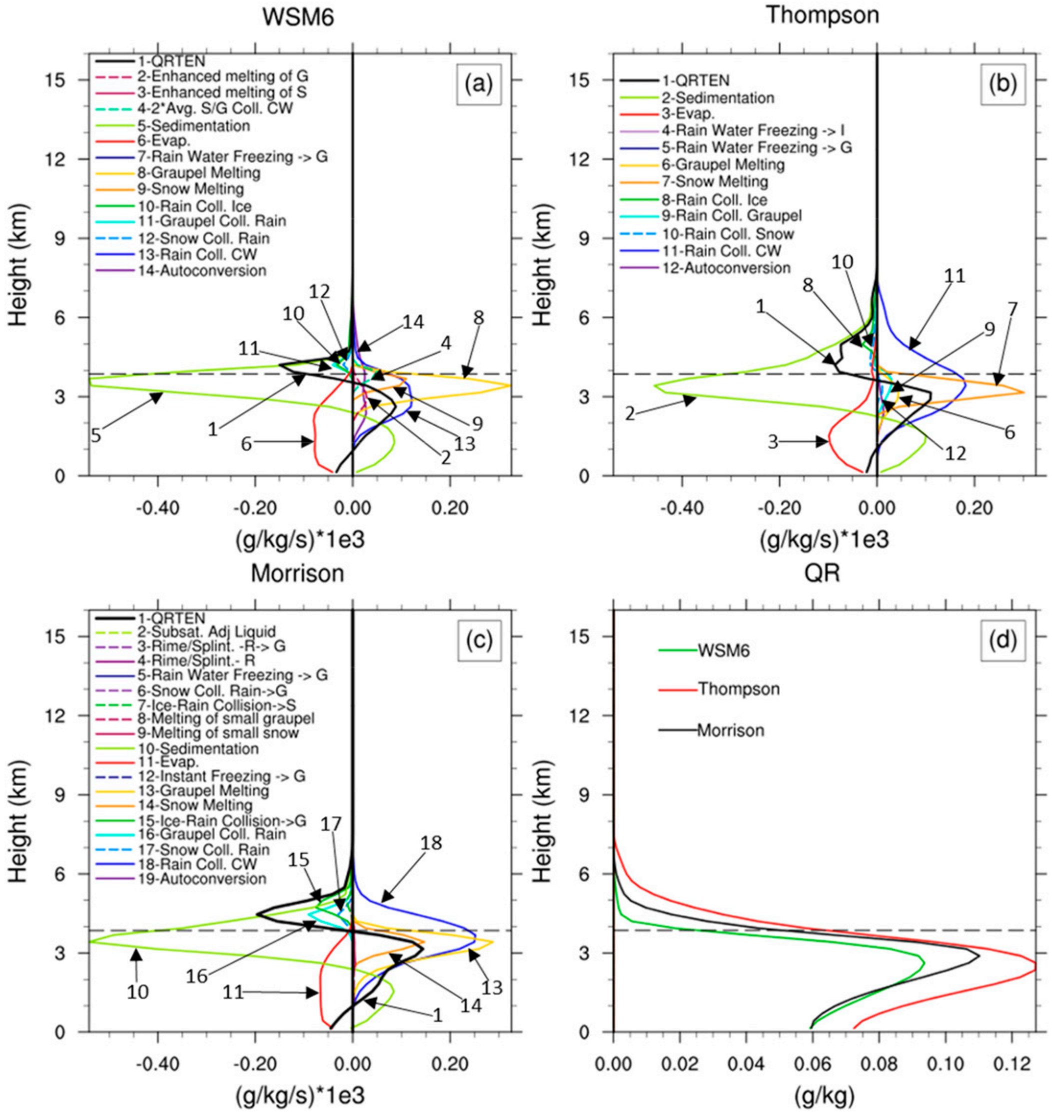

FIG. 16. As in Fig. 5, but averaged over 4–6 h of the simulations. The legends are explained in the Table 2.

rainwater production and evaporation results in the squall lines in the WSM6 and Morrison runs gradually catching up in intensity and development to the run using the Thompson scheme as shown in Figs. 1 and 2. Furthermore, after 2 h, the production of rainwater by graupel melting is reduced in the Thompson run due to the significant reduction of graupel production (mostly due to riming), which is caused by a significant increase in the snow production that increases riming of supercooled cloud water and rainwater onto snow (not shown). Consequently, the contribution to rainwater production by frozen hydrometeor melting is dominated by snow melting in the Thompson run during this time. Between 4 and 6 h, however, the melting of snow in the Thompson run increases significantly because the snow particles grow large enough to fall below the freezing level and melt. As a result, the Thompson run again has a larger quantity of rainwater than the WSM6 and Morrison runs (Fig. 16d). The corresponding cooling by both snow melting and rainwater evaporation results in the increase of the cold pool intensity in the Thompson run during this time shown in Fig. 2.

e. Thermodynamic comparison of microphysical processes

The impact of microphysical process parameterizations on the simulated squall-line development is exerted through their contribution to the cooling that leads to the cold pool development. Figures 17–19 show the

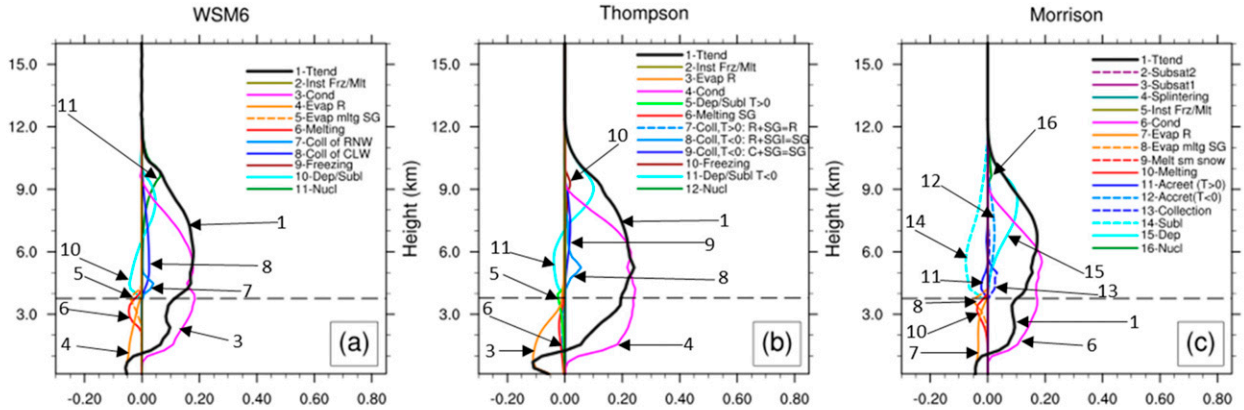

FIG. 17. The area-averaged vertical profiles of the process terms in the tendency equation of temperature due to microphysics averaged over 0–2 h for the (a) WSM6, (b) Thompson, and (c) Morrison runs corresponding to the latent heating profiles associated with microphysics. The black dashed line is the 0°C line. The legend titles are explained in Table 4.

area-averaged vertical profiles of the process terms in the tendency equation of temperature due to microphysics between 0–2, 2–4, and 4–6 h of the simulations. (The legend titles for Fig. 17 are explained in Table 4.) During the first 2 h of the simulations (Fig. 17), the Thompson run has the greatest amount of cooling due to evaporation below the freezing level, corresponding to the greater rain evaporation seen in Fig. 5. One reason for this is that during the first 2 h of the simulations, there is more shedding of rainwater particles in the Thompson run than in the Morrison run when rainwater particles collect graupel below the freezing level, as seen in Figs. 5, 7, and 12. There is no explicit shedding process in the single-moment WSM6 scheme that will lead to a change in the number concentration without a change in total mass. The shedding process of rainwater particles is critical to enhancing evaporative cooling behind the squall line (see more discussion by Morrison et al. 2012). Additionally, the cooling due to melting, mostly of graupel (see Fig. 5) in the Thompson run, takes place over a greater depth than in the WSM6 and Morrison runs during the first 2 h. Since the dominant size of the graupel particles in the Thompson run is larger than in the WSM6 and Morrison runs (Fig. 13) during the first 2 h, it takes more time for the graupel particles to melt in the Thompson run, whereas the smaller graupel in the WSM6 and Morrison runs melt in the 2 km below the freezing level. All these lead to the difference in which there is more evaporation cooling in the Thompson run than the other runs.

After 2 h, the amount of snow in the Thompson run increases enough that a significant portion of it falls below the freezing level and the cooling from melting of snow increases (Figs. 18 and 19). It is important to note that the melting of snow and graupel in the WSM6 and Morrison runs is greater than in the Thompson run during this time due to more fallout of snow and graupel below the freezing level for the former two

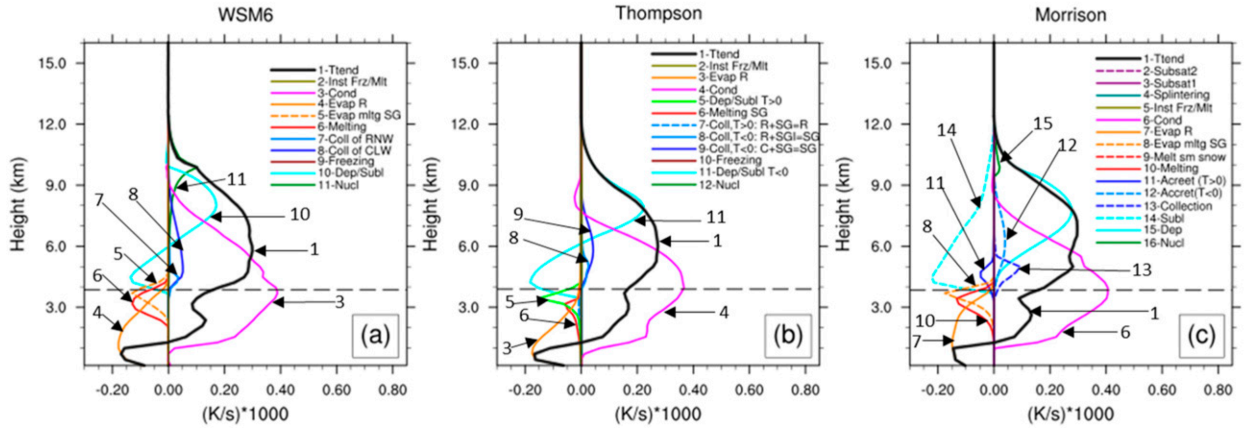

FIG. 18. As in Fig. 17, but averaged over 2–4 h of the simulations.

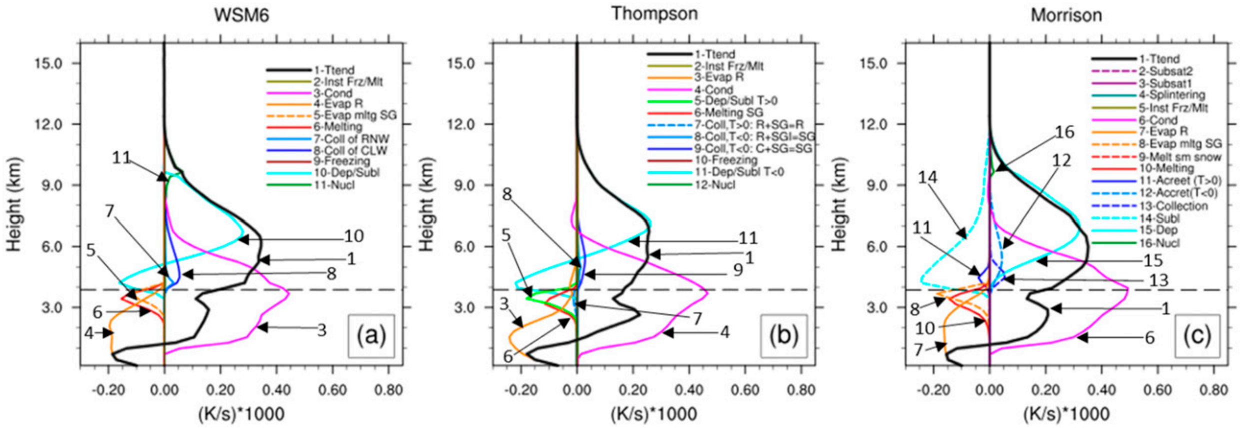

FIG. 19. As in Fig. 17, but averaged over 4–6 h of the simulations.

runs. Also, the depth of the evaporation cooling in the WSM6 and Morrison runs is deeper than in the Thompson run. Nevertheless, the net latent cooling rate below the freezing level in WSM6 and Morrison runs is similar to the Thompson run due to the compensatory feedback by the condensation. Overall, any differences in the cooling below the freezing level between the runs will have a large impact on the development of the squall line because it affects the strength of the cold pool and, consequently, the propagation speed of the squall line.

4. Summary and conclusions

Microphysical pathways to hydrometeor production in three BMSs of the WRF Model are compared in this study using microphysics budget analysis and the physical connection/interaction between the parameterized microphysics processes and the size characteristics of hydrometeor particles for an idealized 2D squall-line case. The results from this idealized case study demonstrate that besides meteorological evaluation of how differently these BMSs perform, the population characteristics of hydrometeor particles simulated by these schemes can also be used to understand the microphysical behavior of individual schemes. They illustrate that there are differences between the schemes in simulated hydrometeor size distributions and physical properties as well as in parameterizations to simulate the net effect of size-dependent processes on subgrid scales such as collection, shedding and collision of hydrometeors. The differences between the schemes reflect current uncertainties in observations and understanding of cloud formation and precipitation production that have long existed. More insightful discussions in this regard can be found in Straka (2009) and Seifert (2011).

This idealized case study shows that the simulated squall-line structure, in terms of the cold pool intensity and the propagation of the gust front, is most sensitive to the sizes of graupel, snow, and rainwater particles and the pathways to their production/reduction. This is consistent with previous observational and modeling studies (e.g., Fovell and Ogura 1988, Rutledge and Houze 1987, and Wu et al. 2013). A more intense squall line is produced during the first 2 h of the simulation in the Thompson run because it produces graupel with larger dominant size, and rainwater particles with smaller dominant size, compared to the other two schemes. This results in more production of rain through graupel melting and thus more evaporation of rainwater during this time in the Thompson run. After 2 h into the simulations, the initially less intense squall lines in the runs using the WSM6 and Morrison schemes start to catch up in intensity and development to the run using the Thompson scheme. This is because graupel particles of smaller dominant size and snow particles in the WSM6 and Morrison runs fall below the freezing level and start to enhance the rainwater production and its evaporative cooling. Meanwhile, during this period, the graupel production in the Thompson run slows down, resulting in less rainwater production and evaporation. As the snow particles in the Thompson run grow large enough to fall below the freezing level and melt, the rainwater production increases again. The above result indicates that between the three schemes, since the difference in the assumed graupel density is small between the schemes (500 kg m^{-3} for both Thompson and WSM6, and 400 kg m^{-3} for Morrison), it is the differences in the simulated dominant size and fall speed of graupel particles that lead to differences in the amounts of rainwater evaporation during the first 2 h in this idealized case. The greater the dominant size of graupel particles, the faster graupel particles fall below the

TABLE 4. The equations for the temperature tendencies due to microphysics for the WSM6, Thompson, and Morrison parameterizations. The numbers in parentheses correspond to the numbers in the legends of Figs. 16–18. The sign (+/−) of the term corresponds to that used in the calculation of the budgets.

WSM6	Thompson	Morrison
Ttend (1) =	Ttend (1) =	Ttend (1) =
+ Instantaneous freezing/melting (2)	+ Instantaneous freezing/melting (2)	+ Phase change due to subsaturation adjustment of any mass mixing ratio, after sedimentation (2)
+ Condensation (3)	− Evaporation of rain (3)	+ Phase change due to subsaturation adjustment of any mass mixing ratio (3)
+ Evaporation of rain (4)	+ Condensation (4)	+ Splintering (4)
+ Evaporation of melting snow and graupel (5)	+ Deposition/sublimation when $T >$ 0°C (5)	+ Instantaneous freezing/melting (5)
+ Melting (6)	− Melting of snow, graupel (6)	+ Condensation (6)
+ Phase changes due to collection of rain by ice, snow and graupel (7)	− Production of rain by rain + snow, rain + graupel collection, if $T \geq$ 0°C (7)	+ Evaporation of rain (7)
+ Phase changes due to collection of cloud water by snow and graupel (8)	+ Collection of rain by snow, graupel and ice to form snow or graupel, when $T <$ 0°C (8)	+ Evaporation of melting snow and graupel (8)
+ Freezing (9)	+ Collection of cloud water by snow, graupel and ice to form snow or graupel, when $T <$ 0°C (9)	− Melting of small snow, graupel (9)
+ Deposition/sublimation (10)	+ Freezing (10)	+ Melting (10)
+ Nucleation (11)	+ Deposition/sublimation when $T <$ 0°C (11)	− Rain production due to accretion of rain by snow or graupel when $T \geq$ 0°C (11)
	+ Nucleation (12)	+ Phase changes due to accretion of cloud water by frozen species when $T <$ 0°C (12)
		+ Phase changes due to collection of liquid by frozen species (13)
		+ Sublimation (14)
		+ Deposition (15)
		+ Nucleation (16)

freezing level and become rainwater through melting to enhance rainwater evaporation. These results are consistent with those found in the study by Gilmore et al. (2004) on the sensitivity of graupel mean size and density in a single-moment scheme. It should be cautioned, however, that if a scheme produces graupel particles that have too great of a density and dominant size in the initial stage of convection development, the large and heavy graupel particles will fall out too fast to melt significantly and affect the cold pool intensification. The ensuing development of the convection and cold pool in this situation will be sustained by the graupel particles of small size and snow particles because they will eventually fall below the freezing level and start to contribute to rainwater production through melting and to enhance the rainwater evaporation. In fact, in the study of the impact of graupel size on bow-echo simulations by Adams-Selin et al. (2013a,b) using the WRF Model, it was found that the graupel particles with smaller mean size and slower fall speed in the WSM6 scheme resulted in a stronger cooling rate behind the gust front after the initial development of convection. The results shown and discussed above indicate that the mean size and fall speed of graupel in the Thompson run are greater than in the other runs, but not as great as the greatest mean size of the graupel in the WSM6 runs presented in the study of Adams-Selin et al. (2013a,b).

This case study is motivated by the recognition that the objective of microphysics parameterization in weather prediction models, like the three schemes presented in this study, is to simulate the mean behavior of the population evolution of hydrometeor particles on subgrid scales and its feedback to the environment based on the behavior of individual hydrometeor particles. As shown in this 2D idealized case study, these schemes may differ quantitatively not only in individual pathways for hydrometeor production via process parameterizations, but also in precipitation and population characteristics of hydrometeor particles as they evolve. Since it remains difficult to measure hydrometeor production processes in nature, it is impossible to observationally validate the individual production processes compared in this study. The results from this study suggest that an alternative way to validate the BMSs in the WRF Model is through the evaluation of prominent hydrometeor production processes in terms of their impact on the hydrometeor size distributions and meteorological processes, which are generally more readily observed in nature than individual microphysics processes of hydrometeor production. It is worth noting that recent studies by Fan et al. (2017) and Morrison et al. (2015) show the trend in research has started moving to this direction. However, it remains important to understand why various schemes in the WRF Model behave differently, and evaluating the differences in individual hydrometeor production terms between the schemes can contribute to this understanding. Finally, it is important to mention that despite the physical insight provided by the comparison results from this study, there are limits in using the 2D idealized squall line for microphysics parameterization evaluation since the interaction between dynamics and microphysical processes in a 2D idealized squall line differs from that in simulations of a 3D real squall-line event. Future studies are needed to address the question of how general the conclusions from this study are by comparing the results to 3D idealized and real case studies.

Acknowledgments. This work is supported by the Next Generation Global Prediction System (NGGPS) Project of NOAA/NWS. The authors also acknowledge the use of the NCAR Command Language (NCL) in the analysis of some of the WRF Model output and the preparation of figures.

REFERENCES

Adams-Selin, R. D., S. C. van den Heever, and R. H. Johnson, 2013a: Impact of graupel parameterization schemes on idealized bow echo simulations. *Mon. Wea. Rev.*, **141**, 1241–1262, https://doi.org/10.1175/MWR-D-12-00064.1.

——, ——, and ——, 2013b: Sensitivity of bow-echo simulation to microphysical parameterizations. *Wea. Forecasting*, **28**, 1188–1209, https://doi.org/10.1175/WAF-D-12-00108.1.

Bao, J.-W., S. A. Michelson, and E. D. Grell, 2016: Pathways to the production of precipitating hydrometeors and tropical cyclone development. *Mon. Wea. Rev.*, **144**, 2395–2420, https://doi.org/10.1175/MWR-D-15-0363.1.

Beheng, K. D., 2010: The evolution of raindrop spectra: A review of basic microphysical essentials. *Rainfall: State of the Science*, *Geophys. Monogr.*, Vol. 191, Amer. Geophys. Union, 29–48, https://doi.org/10.1029/2010GM000957.

Biggerstaff, M. I., and R. A. Houze Jr., 1991: Kinematic and precipitation of the 10–11 June 1985 squall line. *Mon. Wea. Rev.*, **119**, 3034–3065, https://doi.org/10.1175/1520-0493(1991)119<3034:KAPSOT>2.0.CO;2.

——, and ——., 1993: Kinematics and microphysics of the transition zone of the 10–11 June 1985 squall line. *J. Atmos. Sci.*, **50**, 3091–3110, https://doi.org/10.1175/1520-0469(1993)050<3091:KAMOTT>2.0.CO;2.

Bryan, G. H., and H. Morrison, 2012: Sensitivity of a simulated squall line to horizontal resolution and parameterization of microphysics. *Mon. Wea. Rev.*, **140**, 202–225, https://doi.org/10.1175/MWR-D-11-00046.1.

Dudhia, J., S.-Y. Hong, and K.-S. Lim, 2008: A new method for representing mixed-phase particle fall speeds in bulk microphysics parameterizations: Special issue on high-resolution cloud models. *J. Meteor. Soc. Japan*, **86A**, 33–33, https://doi.org/10.2151/jmsj.86A.33.

Fan, J., and Coauthors, 2017: Cloud-resolving model intercomparison of an MC3E squall line case: Part I—Convective updrafts. *J. Geophys. Res. Atmos.*, **122**, 9351–9378, https://doi.org/10.1002/2017JD026622.

Field, P. R., R. J. Hogan, P. R. A. Brown, A. J. Illingworth, T. W. Choularton, and R. J. Cotton, 2005: Parametrization of ice-particle size distributions for mid-latitude stratiform cloud. *Quart. J. Roy. Meteor. Soc.*, **131**, 1997–2017, https://doi.org/10.1256/qj.04.134.

Fovell, R. G., and Y. Ogura, 1988: Numerical simulation of a midlatitude squall line in two dimensions. *J. Atmos. Sci.*, **45**, 3846–3879, https://doi.org/10.1175/1520-0469(1988)045<3846:NSOAMS>2.0.CO;2.

Gilmore, M. S., J. M. Straka, and E. N. Rasmussen, 2004: Precipitation and evolution sensitivity in simulated deep convective storms: Comparisons between liquid-only and simple ice and liquid phase microphysics. *Mon. Wea. Rev.*, **132**, 1897–1916, https://doi.org/10.1175/1520-0493(2004)132<1897:PAESIS>2.0.CO;2.

Han, M., S. A. Braun, T. Matsui, and C. R. Williams, 2013: Evaluation of cloud microphysics schemes in simulations of a winter storm using radar and radiometer measurements. *J. Geophys. Res. Atmos.*, **118**, 1401–1419, https//doi.org/10.1002/jgrd.50115.

Hong, S.-Y., and J.-O. J. Lim, 2006: The WRF single-moment 6-class microphysics scheme (WSM6). *J. Korean Meteor. Soc.*, **42**, 129–151.

——, J. Dudhia, and S.-H. Chen, 2004: A revised approach to ice microphysical processes for the bulk parameterization of clouds and precipitation. *Mon. Wea. Rev.*, **132**, 103–120, https://doi.org/10.1175/1520-0493(2004)132<0103:ARATIM>2.0.CO;2.

Houze, R. A., Jr., P. V. Hobbs, P. H. Herzegh, and D. B. Parsons, 1979: Size distributions of precipitation particles in frontal clouds. *J. Atmos. Sci.*, **36**, 156–162, https://doi.org/10.1175/1520-0469(1979)036<0156:SDOPPI>2.0.CO;2.

Lafore, J., and M. W. Moncrieff, 1989: A numerical investigation of the organization and interaction of the convective and stratiform regions of tropical squall lines. *J. Atmos. Sci.*, **46**, 521–544, https://doi.org/10.1175/1520-0469(1989)046<0521:ANIOTO>2.0.CO;2.

Milbrandt, J. A., and M. K. Yau, 2005: A multimoment bulk microphysics parameterization. Part I: Analysis of the role of the spectral shape parameter. *J. Atmos. Sci.*, **62**, 3051–3064, https://doi.org/10.1175/JAS3534.1.

Morrison, H., J. A. Curry, and V. I. Khvorostyanov, 2005: A new double-moment microphysics parameterization for application in cloud and climate models. Part I: Description. *J. Atmos. Sci.*, **62**, 1665–1677, https://doi.org/10.1175/JAS3446.1.

——, G. Thompson, and V. Tatarskii, 2009: Impact of cloud microphysics on the development of trailing stratiform precipitation in a simulated squall line: Comparison of one- and two-moment schemes. *Mon. Wea. Rev.*, **137**, 991–1007, https://doi.org/10.1175/2008MWR2556.1.

——, S. A. Tessendorf, K. Ikeda, and G. Thompson, 2012: Sensitivity of a simulated midlatitude squall line to parameterization of raindrop breakup. *Mon. Wea. Rev.*, **140**, 2437–2460, https://doi.org/10.1175/MWR-D-11-00283.1.

——, J. A. Milbrandt, G. H. Bryan, K. Ikeda, S. A. Tessendorf, and G. Thompson, 2015: Parameterization of cloud microphysics based on the prediction of bulk ice particle properties. Part II: Case study comparisons with observations and other schemes. *J. Atmos. Sci.*, **72**, 312–339, https://doi.org/10.1175/JAS-D-14-0066.1.

Rutledge, S. A., and R. A. Houze Jr., 1987: A diagnostic modelling study of the trailing stratiform region of a midlatitude squall line. *J. Atmos. Sci.*, **44**, 2640–2656, https://doi.org/10.1175/1520-0469(1987)044<2640:ADMSOT>2.0.CO;2.

Seifert, A., 2011: Uncertainty and complexity in cloud microphysics. *Proc. ECMWF Workshop on Model Uncertainty*, Reading, United Kingdom, ECMWF, 27 pp., https://www.ecmwf.int/sites/default/files/elibrary/2011/14857-uncertainty-and-complexity-cloud-microphysics.pdf.

Skamarock, W. C., and Coauthors, 2008: A description of the Advanced Research WRF version 3. NCAR Tech. Note NCAR/TN-475+STR, 113 pp., https://doi.org/10.5065/D68S4MVH.

Straka, J. M., 2009: *Cloud and Precipitation Microphysics: Principles and Parameterizations*. Cambridge University Press, 392 pp.

Tao, W.-K., D. Wu, S. Lang, J.-D. Chern, C. Peters-Lidard, A. Fridlind, and T. Matsui, 2016: High-resolution NU-WRF simulations of a deep convective-precipitation system during MC3E: Further improvements and comparisons between Goddard microphysics schemes and observations. *J. Geophys. Res. Atmos.*, **121**, 1278–1305, https//doi.org/10.1002/2015JD023986.

Thompson, G., P. R. Field, R. M. Rasmussen, and W. D. Hall, 2008: Explicit forecasts of winter precipitation using an improved bulk microphysics scheme. Part II: Implementation of a new snow parameterization. *Mon. Wea. Rev.*, **136**, 5095–5115, https://doi.org/10.1175/2008MWR2387.1.

Van Weverberg, K., A. M. Vogelmann, H. Morrison, and J. A. Milbrandt, 2012: Sensitivity of idealized squall-line simulations to the level of complexity used in two-moment bulk microphysics schemes. *Mon. Wea. Rev.*, **140**, 1883–1907, https://doi.org/10.1175/MWR-D-11-00120.1.

——, and Coauthors, 2013: The role of cloud microphysics parameterization in the simulation of mesoscale convective system clouds and precipitation in the tropical western Pacific. *J. Atmos. Sci.*, **70**, 1104–1128, https://doi.org/10.1175/JAS-D-12-0104.1.

Wang, P. K., 2013: *Physics and Dynamics of Clouds and Precipitation*. Cambridge University Press, 467 pp.

Weisman, M. L., and R. Rotunno, 2004: "A theory for strong long-lived squall lines" revisited. *J. Atmos. Sci.*, **61**, 361–382, https://doi.org/10.1175/1520-0469(2004)061<0361:ATFSLS>2.0.CO;2.

——, J. B. Klemp, and R. Rotunno, 1988: Structure and evolution of numerically simulated squall lines. *J. Atmos. Sci.*, **45**, 1990–2013, https://doi.org/10.1175/1520-0469(1988)045<1990:SAEONS>2.0.CO;2.

Wu, D., X. Dong, B. Xi, Z. Feng, A. Kennedy, G. Mullendore, M. Gilmore, and W.-K. Tao, 2013: Impacts of microphysical scheme on convective and stratiform characteristics in two high precipitation squall line events. *J. Geophys. Res. Atmos.*, **118**, 11 119–11 135, https//doi.org/10.1002/jgrd.50798.

Xue, L., and Coauthors, 2017: Idealized simulations of a squall line from the MC3E field campaign applying three bin microphysics schemes: Dynamic and thermodynamic structure. *Mon. Wea. Rev.*, **145**, 4789–4812, https://doi.org/10.1175/MWR-D-16-0385.1.